

UC Berkeley

UC Berkeley Electronic Theses and Dissertations

Title

Advances in NMR Methodology

Permalink

<https://escholarship.org/uc/item/65p76076>

Author

Trease, David Richard

Publication Date

2010

Peer reviewed|Thesis/dissertation

Advances in NMR Methodology

by

David Richard Trease

A dissertation submitted in partial satisfaction of the
requirements for the degree of
Doctor of Philosophy

in

Chemistry

in the

GRADUATE DIVISION

of the

UNIVERSITY OF CALIFORNIA, BERKELEY

Committee in charge:
Professor Alexander Pines, Chair
Professor David Wemmer
Professor Steve Conolly

Spring 2010

Advances in NMR Methodology

Copyright 2010

by

David Richard Trease

Abstract

Advances in NMR Methodology

by

David Richard Trease

Doctor of Philosophy in Chemistry

University of California, Berkeley

Nuclear magnetic resonance (NMR) is a powerful spectroscopic technique which has made tremendous advances since its inception 60 years ago. Research in this lab centers on further pushing back the boundaries of this important and fascinating field. The following doctoral dissertation comprises a series of experiments broadly grouped into three chapters, prefaced by a brief introduction.

Chapter one outlines the fundamental principles of magnetic resonance. Chapter two describes the development of two novel techniques for MRI spatial encoding which circumvent the need for conventional pulsed field gradients. Chapter three outlines a series of experiments which probe the fundamental physics of spin relaxation in xenon gas, an important tracer for medical MRI applications. The final chapter covers the progress made so far on the development of a magnetometer based on the diamond nitrogen-vacancy defect and its prospects for use as a cheap, high-sensitivity magnetic field detector for application in nanoscopic NMR imaging.

To mum and dad

Contents

List of Figures	iv
1 Magnetic Resonance	1
1.1 Nuclear Magnetic Resonance	3
1.1.1 Nuclear Spin Polarization	4
1.1.2 Precession	5
1.1.3 Spin Manipulation (or Why a DC Pulse Doesn't Make the Grade)	7
1.1.4 Longitudinal and Transverse Relaxation	8
2 Spatial Encoding Without Magnetic Field Gradients	13
2.1 Magnetic Resonance Imaging	13
2.2 Ultrafast Optical MRI Encoding	14
2.2.1 The Photo-CIDNP Phenomenon	15
2.2.2 The Radical Pair Mechanism	16
2.2.3 Experimental	19
2.2.4 Results	23
2.2.5 Discussion	26
2.3 Spatial Encoding Using Localized Permanent Magnets	27
2.3.1 Local Field Encoding Results	30
3 Xe Relaxation Studies	34
3.1 Ex-Situ NMR	35
3.2 Xe Hyperpolarization	36

3.3	Low-Field Xe Probe Design	36
3.4	Low-Field Gas-Phase Xe Experiments	38
3.5	Low-Field Liquid-Phase Experiments	40
3.5.1	Preparation of Liquid Xenon	41
3.5.2	Relaxation Experiments	41
3.6	High Field Gas Phase Xenon T_2 Experiments	43
4	Diamond NV Magnetometry	48
4.1	Properties of the Diamond NV Center	51
4.1.1	Structure	51
4.1.2	Coherence Lifetime	53
4.1.3	Optically Detected Magnetic Resonance	53
4.2	Experiments	54
4.2.1	Continuous Wave NV Magnetometry With DC Magnetic Field	54
4.2.2	Continuous Wave NV Magnetometry With AC Magnetic Field	58
4.3	Dipolar Field Calculations	63
4.3.1	MATLAB Coding	63
4.4	Prospects	66
	Bibliography	70
A	Appendix	77
A.1	Dipole field calculator	77

List of Figures

1.1	The Zeeman interaction with a spin $1/2$	2
1.2	Precession in a magnetic field. (a) Parallel spin and magnetic field. (b) Spin at an angle relative to magnetic field.	6
1.3	The inversion recovery experiment	10
1.4	The spin echo experiment	11
2.1	(a) Frequency encoding (b) Phase encoding	14
2.2	Initiation of the radical-pair mechanism	16
2.3	Energies in the singlet/triplet basis before (a) and after (b) reaction .	17
2.4	Radical pair mechanism summary	18
2.5	(a) Experimental apparatus (b) Output of light guide.	21
2.6	Modified CSI sequence (omitting presaturation and water suppression pulses). For laser pulse-train experiments, $N=50$. For ultra-fast optical encoding experiments, $N=1$	22
2.7	(a) Structure of DP (b) Dark spectrum <i>vs</i> photo-CIDNP spectrum . .	23
2.8	Coronal images (a) Tripilot guide image of H_2O in solution (b) Guide image with overlayed laser pulse-train photo-CIDNP CSI image. Note the formation of polarization in the region immediately below the quartz rod (c) Single laser-pulse ultra-fast optically encoded image. .	24
2.9	Axial images (a) Tripilot guide image, again showing artifact (b) Guide image with overlayed laser pulse-train photo-CIDNP CSI image, semi- circle shape (c) Guide image with overlayed laser pulse-train photo- CIDNP CSI image, cross-shape	25
2.10	Single laser pulse ultra-fast optically-encoded image. 9×9 resolution. \times	26

2.11	Example "barcode" marking of microfluidic channels, using regions of differing field strength	29
2.12	(a)"Sandwich" of magnetic layers (b) Coiled capillary tubing affixed to masking tape, before casting in epoxy resin	31
2.13	(a) Frequency shift on addition of 1 layer of magnetic disk, in close contact with capillary (b) Successive frequency shifts (right to left) on addition of successive layers of magnetic material.	32
3.1	(a) Duplexer circuitry (b) Pi circuit required at low frequency	37
3.2	Diffusion attenuation enhanced T_2 in Xe gas, in different field gradients	39
3.3	(a) Experimental T_2 decay curve (b) Collation of all liquid Xe T_2 data of which the author is aware	42
3.4	The transverse and surface relaxation rates as a function of $1/a$	46
3.5	Surface relaxivity, M as a function of $1/a$	47
4.1	Cartoon of cantilever-based NV surface magnetometry	50
4.2	Crystal structure of NV center	51
4.3	Energy levels in the NV center	52
4.4	Block diagram of a simple diamond NV magnetometry experiment	55
4.5	Diamond mount	56
4.6	Spectrum of the NV center in varying field strengths, controlled by changing the distance from a rare-earth magnet	57
4.7	Earth's field ODMR spectrum of the NV center	58
4.8	(a) Comparison of direct spectrum and first derivative (b) Phase difference in response of $m_s=+1$ and $m_s=-1$ leading to "emissive" 1st derivative peak	59
4.9	First derivative spectrum at Earth's field	60
4.10	First derivative spectrum at 5 Gauss	60
4.11	NV magnetometer sensitivity to DC magnetic field	61
4.12	NV magnetometer sensitivity to AC magnetic fields	62
4.13	Cartoon of the envisioned position of the NV diamond relative to the water channel	64

4.14	(a) Diagram of the field map geometry (b) x component of magnetic field (c) z component of magnetic field (d) magnitude of magnetic field. NB due to the geometry of the simulation the y component of the field was zero at all points	65
4.15	Spin echo pulse sequence suitable for pulsed NV magnetometry experiment	67
4.16	Block diagram of the pulsed NV magnetometry experiment	68

Acknowledgments

It is fascinating to observe how one’s path through life is the result of seemingly arbitrary choices, often made upon a whim. The winding route that has led to the writing of this dissertation is a case in point. Why chemistry? Why Ph.D.? Why the USA? Why NMR? A different decision at any of these many junctions would have placed me thousands of miles away from Schmidt’s Tobacco Trading Company and Pub in Berkeley, where I am currently positioned, writing this.

And at every point there has been a person or persons guiding, helping and influencing me, whether or not they realize their significance. I remember vividly my first brush with the true beauty of science — talking with my father whilst walking along the dockside in a small scottish fishing village. I was 12 years old and dad was telling me about Einstein’s grand unified theory. A scientific theory to explain *everything*. The scale of the undertaking and the wonder of the mere possibility of such a thing blew my mind. From then on, I think, I was a scientist. Ultimately, my choice of chemistry was made thanks to Mr Scholes of Vyners School who claimed that getting into Oxford would be “easy”. I don’t resent him for subsequently telling his classes that I was “a bit odd”. It was Dr Battle at Oxford who gave me the sense that the scientific world was my oyster. Berkeley was a choice made thanks to the wonderful influence of Miss Katherine McDowell, to whom I owe more than I can put into words. And, of course, my choice of NMR was made thanks to Alex Pines, whose persuasive powers are almost as legendary as his huge contribution to the field.

It goes without saying, but it shall be said anyway, that I thank my family for all their support throughout my US adventure; Phil for his great enthusiasm about my scientific career; Claire for listening and advising me through some of the tougher times here; dad for inspiring me and grounding me in logic and reason; and mum for her kindness and endless support in everything I do.

My time in the Pines lab has been a gift to me, regardless of the inevitable ups and downs that have occurred therein. It has been an honor to work with so many of the brightest minds in science in such a positive and creative atmosphere. I would like to specially thank Alex for enabling such an environment to flourish and for encouraging me to be a part of that; Vik for instigating and overseeing much of what I have achieved here — his tenure has been at least in part responsible for the most positive environment that I have encountered in this lab; and Chip, whose friendship and warmth brightened the harder times I have had in the US. I should also mention Jeff, Nick, Claudia and Victor with whom I worked closely to generate the results given in the following chapters.

Finally, I’d like to acknowledge those experiments that never made it. This dissertation comprises only the experiments that were run in the last two years of my Ph.D. The macroscopic qubits never quite coupled strongly enough. Laser-pulsed

PASADENA recycling was just out of reach and the rotating magnet proved a little too inhomogeneous for NMR. However, the beauty of research, particularly in the Pines lab, is that when something fails there are always a thousand other possible experiments to run and a hundred other brilliant people with whom to collaborate.

Chapter 1

Magnetic Resonance

“I have not yet lost a feeling of wonder, and of delight, that this delicate motion should reside in all the ordinary things around us, revealing itself only to him who looks for it.”

E. M. Purcell, Nobel Lecture, 1952

Magnetism is a phenomenon that many of us encounter at a young age. Playing with simple bar magnets as a child, there are some aspects to this mysterious force that immediately become apparent; some parts of magnets attract whilst others repel; and the force is strong — enough to pinch small fingers in between blocks. For most of us, this is where our exploration of magnetism stops. It remains a strange but otherwise insignificant curiosity. It is thus a surprise to find, as an adult, that magnetism is prevalent within all things. Water is magnetic. Even air is magnetic. Possibly stranger still is the fact that the source of this magnetism is the same for all of these objects: quantum mechanical spin.

In the heyday of quantum mechanics strange new results and predictions were *de rigueur*. But few predictions have remained as strange and anti-intuitive as Paul Dirac’s prediction of the property known as spin. Simply put, fundamental particles such as the proton and electron have angular momentum. This can be envisioned as the particle spinning on its axis, like a top. However, whilst this is a useful analogy, it is ultimately incomplete. The angular momentum is an intrinsic property of the particle. It simply *has* angular momentum. It does not spin in any sense that we can intuitively understand (in fact, assuming the nucleus to be a hard sphere, if it really were spinning, the velocity at the surface would be much greater than the speed of light!)

So far, this is no explanation for the presence of magnetism. However, analogous to the way that a moving charge generates a magnetic field (for example, a current of

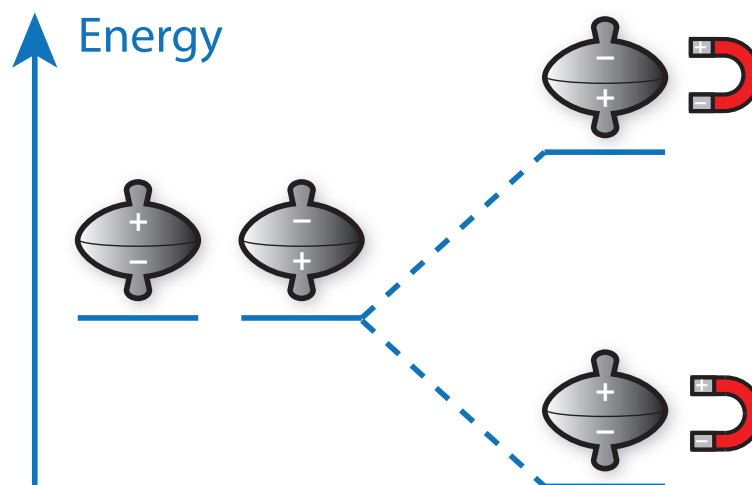


Figure 1.1: The Zeeman interaction with a spin $1/2$

electrons in a wire) a spinning charged particle is also magnetic. It is said to possess a "magnetic moment". The orientation of this magnetism is along the spin axis of the particle. To complete the classical analogy, we can view an electron or proton as a tiny spinning bar magnet. In most materials, electron spins are paired up in opposite directions, so that their magnetic moments cancel. In certain materials, however, the electrons are unpaired and point in the same direction. It is the combined effect of countless quintillions of these nanoscopic magnetic moments lining up together that enables children to observe the fascinating patterns created by running a horseshoe magnet over a bed of iron filings.

Beyond entertaining schoolchildren and affixing notes to a fridge there is a more subtle way of exploiting the properties of magnetic particles which relies on the inherently quantum mechanical nature of spin. This is the field of research known as magnetic resonance and comprises three main areas; nuclear magnetic resonance (NMR); electron paramagnetic resonance (EPR); and magnetic resonance imaging (MRI). Of the three, this dissertation will concentrate on NMR and MRI, although electron paramagnetic resonance is significant in some of the experiments detailed.

Spin is a quantum mechanical property. This means that the available spin energy levels are constrained to specific, discrete values. For the vast majority of cases in this dissertation, we are going to deal with the simplest possible spin system: the spin $1/2$. A spin $1/2$ particle has only two possible spin states: spin up ($+1/2$) or spin down ($-1/2$). Recall that the magnetic moment is aligned with the spin. So we can envision spin up as a magnet spinning with its south pole in contact with a table and

spin down as the magnet spinning with its north pole in contact with the table. Now, in the absence of any other magnetic fields our spinning top will keep on happily spinning on its tip forever. The spin-up and spin-down states are described as being equal in energy, or *degenerate*. However, let us now introduce another magnetic field by, say, bringing a big bar magnet up close to our little spinning top. Depending on its alignment the top will either feel a force helping it to stand up or one that makes it want to topple over. The spin-up and spin-down states are no longer equal in energy. This is shown pictorially in figure 1.1 The energy difference introduced by applying the external magnetic field is known as the *Zeeman splitting* and is given by

$$E_{Zeeman} = -\gamma\hbar B_0 \quad (1.1)$$

where \hbar is the reduced Planck's constant, γ is the gyromagnetic ratio (radian/T) of the spin and B_0 is the strength of the applied magnetic field (T).

We can observe the Zeeman splitting simply by applying radio waves of different frequency (and therefore different energy) to the sample of interest and seeing which frequency is absorbed most. This frequency is known as the resonant excitation energy. Hence the 'resonance' in magnetic resonance.

The size of this energy difference tells us what magnetic field the particle of interest is experiencing. Simply by finding out the size of the Zeeman splitting, it is possible to determine the chemical environment of a nucleus or look with high resolution into the human body. However, there is much more to magnetic resonance than just this, as we shall see in the following chapter.

1.1 Nuclear Magnetic Resonance

In the past 60 years, magnetic resonance has developed from a fascinating curiosity of atomic physics into one of the most powerful spectroscopic tools available. To the chemist, NMR is generally encountered in undergraduate classes as a tool for determining the nature and purity of the products of organic chemistry. The biochemistry undergrad will meet NMR in its incarnation as one of the very limited number of tools available for protein structure determination. The medical student will see NMR as part of the complicated physics underpinning the MRI experiment. In truth NMR is all of these things and more. Its applications extend far beyond, into nanomaterials, oil prospecting and even art restoration!

The vast majority of the research carried out in the field of magnetic resonance involves the atomic nucleus. Even though the atomic nucleus is typically composed of multiple protons and neutrons, each with their own spin, the nucleus is well de-

scribed using a single spin, resultant from sum of the spins of the individual nucleons. Nuclear spin has a number of attractive qualities for its use in scientific experimentation. Amongst the most important is that it is only very weakly coupled with its surroundings, collectively known as the lattice. Commonly nuclear spins show quantum coherence lifetimes of seconds and, in some exotic cases [52], much, much longer. This property allows their use in very-high resolution spectroscopic experiments, as spectroscopic linewidth is inversely proportional to lifetime.

Nuclear spins are ubiquitous. And whilst not every nucleus possesses a magnetic moment, the most abundant element in the universe, H, has the close to the largest magnetic moment of all the elements. It is interesting to muse on the fact that the usefulness of NMR largely stems from essentially a happy accident — the most interesting nucleus to study also has the highest NMR signal. If nature had conspired to give the heavy elements a large nuclear spin and the light ones a small spin, NMR would be an experimental oddity, applicable to only a few specialized systems.

1.1.1 Nuclear Spin Polarization

As with every form of spectroscopy, the advantages of using NMR come only with concomitant drawbacks. The greatest enemy to the spectroscopist comes in the form of poor signal to noise. This is a direct result of poor ensemble polarization.

In an NMR experiment we are essentially measuring the amount of nuclear magnetization in a sample. Unfortunately we don't have the sensitivity to detect the magnetization from a single nuclear spin (yet!) [53]. Instead we look at the net magnetization of a macroscopic volume of sample, commonly a few mm³, containing of the order of 10¹⁷ nuclear spins. However, not all of these spins are oriented in the same direction. In fact in the absence of any external magnetic field there is no preferred direction at all. This means that in a zero-field NMR experiment the magnetic moments essentially cancel each other out, giving us no NMR signal whatsoever. In order to create a preferential orientation for the nuclear spins we must apply an external magnetic field to lift the degeneracy of the spin energy levels (see equation(1.1).)

At temperatures above a few hundredths of a degree Kelvin the available thermal energy is greater than the Zeeman splitting, resulting in very small polarization of the system. The degree of polarization is linear in the size of the applied magnetic field, one of the reasons for the drive to bigger and bigger magnets. The excess of spin "up" over spin "down", as a fraction of the overall population is given by,

$$P = \frac{\hbar\gamma B_0}{2kT} \quad (1.2)$$

where k is the Boltzmann constant and T is the temperature.

Even in the strongest NMR magnet currently available, 23.5 Tesla, the nuclear polarization of protons is equivalent to about one nucleus in five thousand. This thermal polarization 'deficit' has driven research into ways of overcoming it. Together, these are known as *hyperpolarization* methods and are outlined below:

PASADENA (Para-Hydrogen And Synthesis Enable Dramatically Enhanced Nuclear Alignment): This technique takes advantage of the high spin-order in para-hydrogen. When purified and then added to a substrate molecule, the para-hydrogen nuclei can be manipulated into a pure state, with 100 % NMR polarization.

DNP (Dynamic Nuclear Polarization): Due to the much greater gyromagnetic ratio of the electron, electronic polarization is much greater than nuclear polarization (this is even more pronounced at low temperature). DNP techniques transfer some of that polarization through space to nearby nuclei.

Noble gas hyperpolarization: Noble gases such as He, Xe are not reactive and are stable in their atomic forms. Lack of coupling with the nuclei allows for very long polarization lifetimes. Because of these factors, noble gas nuclei can be polarized in the harsh conditions of an alkali metal vapor cell. High laser powers, often greater than 100 W, polarize the alkali metal valence electron. This polarization is then transferred collisionally to the noble gas. With this technique, polarizations in tens of percent are obtainable.

CIDNP (Chemically Induced Dynamic Nuclear Polarization): Certain chemical reactions show a significant enhancement in the nuclear polarization of the products. This technique is utilized more for spin-labelling rather than for hyperpolarization and is detailed in Chapter 2.

1.1.2 Precession

Unfortunately, the completely intuitive picture of magnetic resonance only takes us so far. The magnetic resonance experiment broadly outlined at the beginning of the chapter, where the RF frequency is swept across the spectrum recording which energy is most strongly absorbed, is known as continuous wave NMR. This was more or less the only game in town as far as NMR experiments were concerned until the 1970s when pulsed NMR was born. The pulsed NMR revolution has rendered continuous wave (CW) NMR more or less obsolete (although there are some ingenious new ideas for implementing Hadamard-encoded CW experiments [36]). Modern NMR spectrometers use short, high-power radio frequency pulses to delicately manipulate the nuclear spins. The physical dynamics of what happens when we put a tiny spinning nucleus in a large magnetic field and apply a radio-frequency field to it require a slightly more methodical approach than has been given so far.

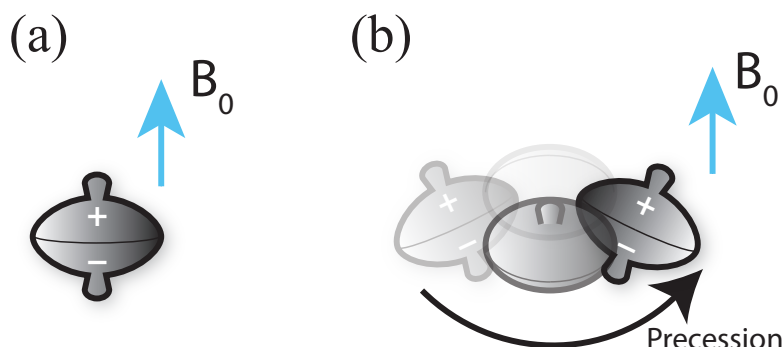


Figure 1.2: Precession in a magnetic field. (a) Parallel spin and magnetic field. (b) Spin at an angle relative to magnetic field.

Conveniently for the NMR scientist, much of the basic physics of NMR can be understood from a classical point of view. For this we can return to our magnetic spinning top. When the axis of the top is parallel with an applied force (in the case of the spinning top this is the force of gravity, in the case of a nuclear spin this is magnetism) there is no motion other than the spin on the rotational axis. However, apply a force at an angle with the rotational axis and the top will begin to precess around it. (Figure 1.2). In NMR the rate of precession of a nucleus in a given magnetic field is called the *Larmor frequency*, ω and is given by

$$\omega = \gamma B_0 \quad (1.3)$$

At this point it is interesting to bring up the question: given that the field of the superconducting magnet is in the range of a few Tesla, whilst the total field of our sample is, at very best, a few nanotesla, how is it possible to detect nuclear spins in an NMR magnet? This would require a magnetic field detector with a dynamic range of 9 orders of magnitude, making this a difficult experiment, to say the least! However, if we instead look not for absolute magnetization but for the small oscillating field generated by the precession of the spins then things become much easier. An oscillating magnetic field induces a current in a coil of wire through the mechanism of Faraday induction, whereas a static field, no matter how large, induces no current at all. Thus, in a conventional NMR experiment we use a small coil of wire to detect the oscillating magnetic field caused by the precession of countless trillions of nuclear spins. The voltage induced in a coil due to an oscillating magnetic field is proportional to the square of the frequency. Given that the Larmor frequency in a superconducting magnet is of the order of hundreds of MHz, then our tiny precessing nuclear magnetic

field shines through, even in the presence of a substantially greater static field.

1.1.3 Spin Manipulation (or Why a DC Pulse Doesn't Make the Grade)

We now know how to detect nuclear magnetism when it is precessing in a plane perpendicular to the applied magnetic field. However, when we put our sample into the NMR magnet, the nuclear spins orient themselves *parallel* with the magnetic field.

Thus we must somehow manipulate the spins' directions. We do this by applying a radiofrequency (RF) pulse. An RF pulse oriented in the x direction can be modeled for our purposes as a magnetic field whose magnitude varies with time

$$B_1(t) = \vec{x}A \sin(\omega t) \quad (1.4)$$

where B_1 is the amplitude of the magnetic field at time t , \vec{x} is the unit vector in the x direction, A is the maximum amplitude of the RF pulse, ω is the frequency of the RF field and t is time. Note that the RF field, B_1 is given the subscript, 1, to distinguish it from the static field B_0 .

We can split this into two counter-rotating components:

$$B'_1(t) = 1/2(\vec{x}A \sin(\omega t) + \vec{y}A \cos(\omega t)) \quad (1.5)$$

$$B''_1(t) = 1/2(\vec{x}A \sin(\omega t) - \vec{y}A \cos(\omega t)) \quad (1.6)$$

One of these components, B_1 , rotates with the nuclear spin and is described as on-resonant with the Larmor precession of the nucleus. The other is 2ω off-resonant from the Larmor precession and can be ignored in high magnetic fields where ω is large.

When we apply the RF field to the nuclear spin, it begins to precess around B_1 . This precession tips the spin slightly and it now begins to also precess around B_0 . However, as B'_1 rotates at the precession frequency, the spin orientation always remains perpendicular to B'_1 . If we continue to apply an RF field, the spin traces a spiral shaped path through space, gradually heading towards the x,y plane. Applying a small DC pulse perpendicular to the spin achieves nothing, as the precession around B_0 averages its evolution around the DC pulse to zero.

The presence of two axes of rotation is hard to visualize and its typical to make the *rotating frame transformation*. The static Cartesian axes x,y and z are not necessarily

the most convenient to use. Here it considerably simplifies matters if our axes actually rotate with the Larmor precession of the nucleus. This is akin to the difference between watching a rotating merry-go-round from a distance and actually sitting on it. Initially you view the merry-go-round spinning around, then, when you climb aboard, the merry-go-round appears stationary and it is rest of the world that is spinning. Thus, in the rotating frame, a spin undergoing Larmor precession appears stationary, whilst a spin which is stationary in the lab frame appears to be precessing in the opposite sense in the rotating frame.

In the rotating frame an RF pulse induces the nuclear spin to trace an arc from the z axis down to the xy plane. If the RF pulse continues, eventually the spin ends up antiparallel with z , then traces its path back to the xy plane. This process is called nutation. The point at which the RF pulse is turned off is known as the flip angle. Assuming that there is no loss in magnetization during the experiment, the magnetization vector traces a line on the surface of a sphere. This is termed the Bloch sphere.

The coil used in an NMR experiment detects the transverse component of precession (ie the projection of the magnetization onto the xy plane in the Bloch sphere only). Thus, signal is maximized if the magnetization vector is rotated onto the xy plane. This corresponds to a flip angle of 90 degrees. Most NMR experiments begin with a 90 degree pulse, in order to maximize the NMR signal. A notable exception is the PASADENA experiment where signal is maximized by a 45 degree pulse.

The voltage induced in the coil oscillates at the same rate as the precessing magnetization. This is called the free induction decay. The amplitude of this voltage is directly proportional to the size of the magnetization in the sample. Thus, the induced voltage gives us information about the density of nuclear spins in the sample. However, it does much more than just this. The oscillating voltage is the sum over the magnetization of every precessing spin. Each spin precesses with a characteristic frequency due to its local chemical environment. The effect on the precession frequency due to these intramolecular effects is called the chemical shift. If we take a Fourier transform of the free induction decay we obtain the frequency domain spectrum which, in general, gives a much clearer picture of the spectrum of precession frequencies.

1.1.4 Longitudinal and Transverse Relaxation

So far, in this rather brief account of NMR, everything has been described in the absence of *relaxation*. Thus it would appear that once a nuclear spin has been tipped into the transverse plane, it will apparently continue precessing forever. This is absolutely not the case; entropy and the return to thermal equilibrium dominate

NMR experiments. There are two relaxation processes at work whenever an NMR experiment is run; longitudinal and transverse relaxation.

Longitudinal relaxation is the process whereby a spin system returns to thermal equilibrium after some kind of excitation. Following an excitation pulse — let's assume a 180 degree pulse - the spin system has essentially undergone a population inversion, from spin up to spin down. The spin system is no longer in thermal equilibrium - in fact it now technically has a negative temperature! However, it will not stay this way forever. The mechanisms for return to thermal equilibrium differ depending on the nature of the system being studied. For systems in the liquid state, relaxation is dominated by modulation of the local magnetic field by nearby magnetic nuclei diffusing through solution. If this modulation is at the resonant frequency of the Zeeman transition, it will induce spin flips, taking the system back to thermal equilibrium.

Longitudinal relaxation is given by

$$M_z(t) = M_z(0)(1 - e^{-t/T_1}) \quad (1.7)$$

where $M_z(t)$ is the z magnetization at time, t and $M(0)$ is the initial magnetization. longitudinal relaxation is characterized by the parameter, T_1 , and the process of longitudinal relaxation is often referred to simply as “ T_1 relaxation”.

In a liquid or gas, the modulation rate is proportional to the translational energy of the molecules; faster moving nuclei lead to higher modulation frequencies. The upshot of this is that the temperature dependence of T_1 can be unexpected! For example, the distribution of translational energies of molecules in solution has the familiar Boltzmann shape. At room temperature the peak of the distribution lies at a higher translational energy than that required for a water molecule to effectively induce proton spin flips at 300 MHz. As temperature is increased, the peak moves to successively higher energies and the proportion of water molecules with the correct translational energy drops. Thus, rather anti-intuitively, the T_1 of a proton in aqueous solution *increases* with increasing temperature!

In order to measure the value of T_1 we typically run an inversion recovery experiment (Figure 1.3). An initial 180 is followed by a delay, τ . During the delay period the ensemble of spins begins to relax back to thermal equilibrium. A 90 pulse turns the polarization into an observable coherence. By arraying the parameter τ a curve of $M(t)$ vs t is created. This is an example of a simple 2-dimensional experiment, where we observe the evolution of the nuclear spins in an indirect dimension.

The other relaxation process of importance in the NMR experiment is transverse relaxation. This is the gradual decrease in magnetization in the xy plane after an excitation pulse. It is the result of the tiny differences in local magnetic field for

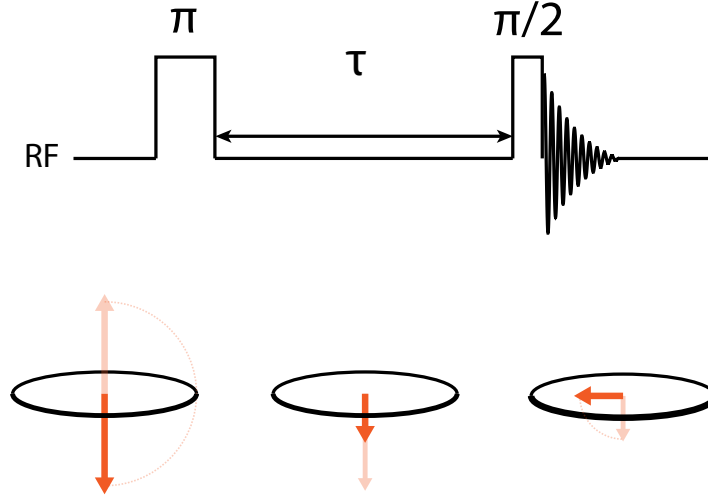


Figure 1.3: The inversion recovery experiment

each individual spin. Immediately following a 90 degree excitation, the nuclear spins are in a coherent state; they all point in the same direction. Now that they are perpendicular to the large static field they begin to precess. If each spin experienced exactly the same magnetic field then they would continue to precess coherently until T_1 relaxation returned the ensemble to thermal equilibrium. In reality, this is not the case, and each spin experiences a slightly different field from the others. Thus the ensemble of spins begins to lose coherence, as each tiny magnetic moment fans out from the ensemble.

Transverse relaxation is given by

$$M_{xy}(t) = M_{xy}(0)e^{-t/T_2} \quad (1.8)$$

where $M_{xy}(t)$ is the transverse magnetization at time, t and $M_{xy}(0)$ is the initial transverse magnetization. It is characterized by the variable, T_2 , and the process of transverse relaxation is often referred to simply as “ T_2 relaxation”.

The requirement for a homogeneous magnetic field is now explained — it is imperative for spins in different spatial locations to experience the same magnetic fields. Any inhomogeneity in the magnetic field leads to more rapid decoherence. It is, however, possible to “recohere” the decoherence due to inhomogeneities in the magnetic field. This was first realized by Erwin Hahn in his celebrated *spin echoes* paper [26].

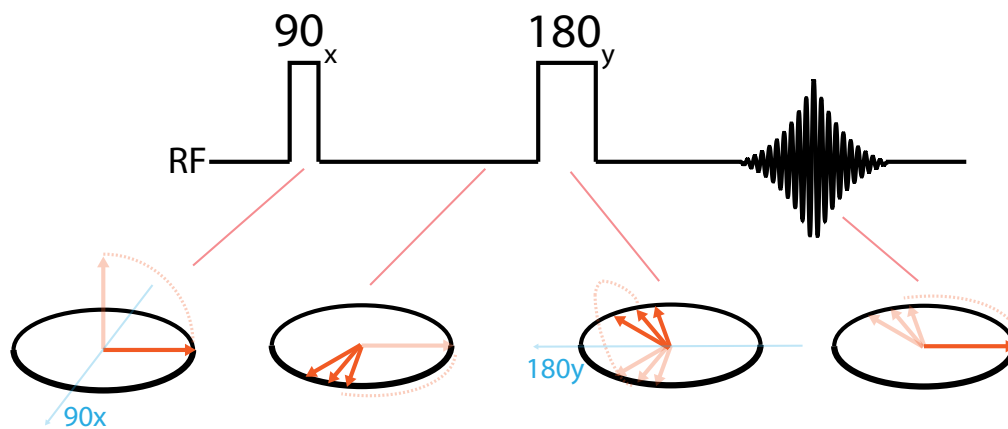


Figure 1.4: The spin echo experiment

Simply by adding an additional 180 pulse following a 90 pulse, the nuclear spin magnetization is seen to "return from the dead". The explanation is quite simple; following the 180 pulse, the spins evolve under a Zeeman Hamiltonian essentially with the opposite sign. After a time, τ , they recombine in the same state that they were in immediately following the initial 90 excitation (Figure 1.4).

Upon closer examination, the timing of the first spin echo experiment, 1950, is surprising — it appears to be an inherently pulse based technique. Was Erwin Hahn so ahead of his time that he was running pulsed NMR 20 years before his peers? The answer is both a yes and a no. Hahn was not running a pulsed NMR experiment as we know today. He was initially studying T_1 in an inversion recovery-type experiment with very long pulses, closer to what we would consider today to be adiabatic excitations. The realization of the broadband nature of a hard NMR pulse was still some years away. Nevertheless, it is with some amusement that Hahn recalls colleagues at the time telling him that pulsed NMR was a dead-end [27]; he feels that discovering the spin echo was probably worthwhile!

The Hahn echo, while powerful, only refocuses decoherence due to magnetic field inhomogeneities. The T_2 due including refocusable decoherence is generally called T_2^* . The envelope of a train of Hahn echoes is the unrefocusable decay, the true T_2 .

It is worth mentioning that relaxation is not inherently a bad thing. The rate of T_1 and T_2 relaxation gives us valuable information about the local environment in which the spins are situated. Local paramagnetic materials, changes in molecular degrees of freedom and temperature changes all influence the relaxation properties of nuclei. This information can be used in a multitude of ways; to determine the proportion of

oil to water in oil wells [\[31\]](#), to extract diffusion constants [\[32\]](#) or, as is now being researched by at least two startup companies (T2 biosystems and NanoNMR), to act as a reporter for chemical binding events.

Chapter 2

Spatial Encoding Without Magnetic Field Gradients

2.1 Magnetic Resonance Imaging

Paul Lauterbur's paper on "zeugmatography" failed to cause a great stir in the NMR world when it was published in 1973 [37]. He outlined a way in which spatial information could be encoded into the precession frequency of nuclear spins. It was certainly inconceivable to most that this work would spark a research field which would one day overcome NMR in scale and, arguably, importance.

Today MRI is a multi-billion dollar medical industry employing tens of thousands of engineers and medical professionals. It has become an invaluable tool for the understanding and diagnosis of disease. Driven primarily by investment by the US medical industry, research and development continues apace, where small improvements in signal to noise and spatial resolution can make big impacts in the field. More recently, functional MRI (fMRI) has been used to give spectacular insights into the function of the brain.

Spatial encoding in an MRI experiment typically consists of frequency and/or phase encoding steps. The simplest of the two to understand, used by Lauterbur in his initial experiments, is frequency encoding (Figure 2.1(a)).

If a field gradient is applied across an object, the nuclear spins will no longer precess at the same Larmor frequency. Those in a stronger total field will precess more rapidly than those in a weaker total field. If the field gradient is applied during acquisition of the FID, the spectrum of the sample in an NMR experiment will be a 1D projection of the object. This is the basis of frequency encoding. As an extension to the frequency encoding method, it is possible to selectively excite a single region

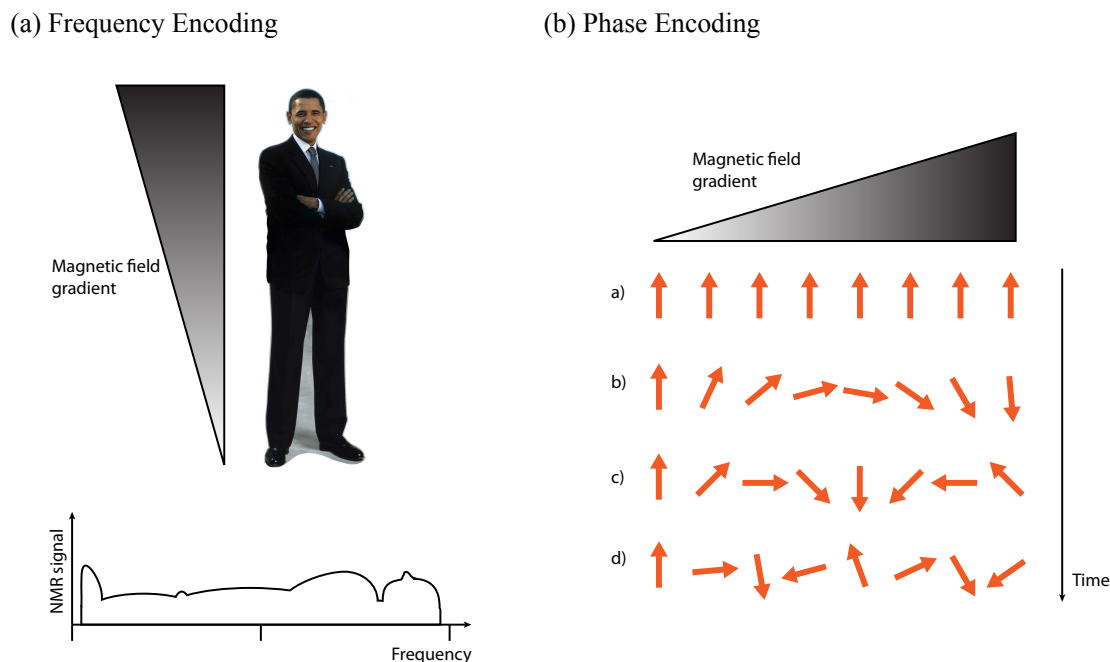


Figure 2.1: (a) Frequency encoding (b) Phase encoding

of the sample by applying a frequency-selective RF pulse whilst the gradient is on.

Frequency encoding can provide a one shot 1D image but in order to more quickly acquire 2D MRI images it can be necessary to apply a phase encoding step as well (Figure 2.1(b)). In comparison to the frequency encoding technique, in which a gradient is applied during acquisition, phase encoding requires a gradient pulse before acquisition. Over the duration of the gradient pulse, the spins evolve at a spatially dependent Larmor frequency. Consequently, following the pulse, the spins have acquired a spatially dependent phase factor. By arraying the phase encode duration, and taking the Fourier transform, spatial information about the sample can be reconstructed.

2.2 Ultrafast Optical MRI Encoding

MRI differs from optical microscopy in that it is capable of peering deep within unmodified and unlabeled materials, elucidating their structure on length scales from micrometers to meters and their dynamics on time scales from microseconds to sec-

onds. In comparison with optically-detected spectroscopic techniques, however, MRI has much lower sensitivity and temporal resolution, complicating its application in studies of dynamical processes that occur in less than 100 microseconds. These limitations motivate the development of hybrid optical-MRI techniques that combine the properties of optical detection with those of NMR for polarization [67], detection [9], and now encoding.

Because of limitations in gradient circuits, the gradient in an MRI experiment is almost always applied for several milliseconds, limiting the time resolution of the experiment. While recent experiments employing remote detection of flowing fluids have achieved time resolution in the few microsecond range [28], they do so at the expense of an additional spatial dimension in which the temporal information is encoded and are thus ultimately limited by magnetic field gradients and flow dynamics.

In the following chapter we exploit the phenomenon of photo-CIDNP to spatially encode nuclear spins on a microsecond timescale [61]. In photo-CIDNP, hyperpolarization of the nuclear spins occurs because of a photochemical reaction that proceeds through spin-correlated radical pair intermediate, as outlined below. The pattern of spin polarization reflects the pattern of initiating optical radiation, and hence a relevant medium solid or liquid can be encoded at a resolution limited by optical diffraction by shaping the light irradiated on the sample.

2.2.1 The Photo-CIDNP Phenomenon

In the early 1960s it was first observed that large, non-equilibrium, nuclear spin polarizations could result from certain chemical reactions [69]. It was initially thought to be a dynamic nuclear polarization phenomenon, whereby spin polarization was being transferred from paramagnetic radical electrons to nuclei via the dipolar coupling. Thus the process was named CIDNP (Chemically Induced Dynamic Nuclear Polarization.) However, gradually it was realized that the generation of the polarization was of a more subtle nature than polarization transfer. In fact, CIDNP is mainly spin-sorting process, whereby the products of a reaction are influenced by the initial nuclear spin state. The acronym remains with us, however, a historical testament to the original experiments.

In the 1970s, Kaptein showed that the CIDNP effect could be observed for a number of photochemically initiated reactions [34]. Of particular interest was a class of reactions where polarization was enhanced for tryptophan, tyrosine and histidine residues on a protein. It was realized that this could be used as a probe for solvent accessible residues on a protein. Gradually photo-CIDNP, as it is called, has come to dominate the field, such that over the last 10 years, only about 15 % of publications have come from studies of thermal CIDNP [23].

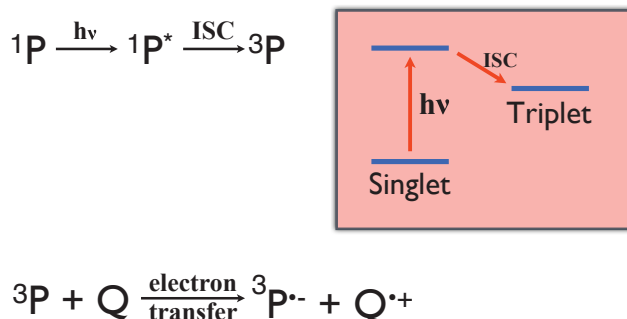


Figure 2.2: Initiation of the radical-pair mechanism

Photo-CIDNP and the wider significance of the radical pair mechanism is still an area of active research, for applications such as the elucidation of protein folding dynamics [45], as a fast solution-state hyperpolarization technique [57] and in solid-state hyperpolarization studies [73] [66].

2.2.2 The Radical Pair Mechanism

The pattern of absorptive and emissively-phased peaks in the CIDNP spectra was initially something of a mystery to researchers. The prevailing DNP model struggled to predict this pattern, which eventually led to its complete rejection in favor of the *radical pair mechanism*. The radical pair mechanism explains the surprising fact that in a chemical reaction, nuclear spins, with energy levels orders of magnitude away from the electronic energy levels which determine reactivity, can influence the outcome. There are a number of excellent reviews of this topic. Particularly recommended for its relevance to these experiments is Hore and Broadhurst’s *photo-CIDNP of Biopolymers* [30].

The mechanism starts with the excitation of a molecule, P, from an electronic singlet (S), with no unpaired electron spins, to a triplet (T), a diradical,



In a thermal CIDNP experiment this excitation is provided by chemical excitation; in a photo-CIDNP experiment this is an optical excitation that probably occurs via a short-lived singlet state (Figure 2.2). The triplet molecule goes on to react with another species in solution, Q, via electron transfer, generating a geminate pair or

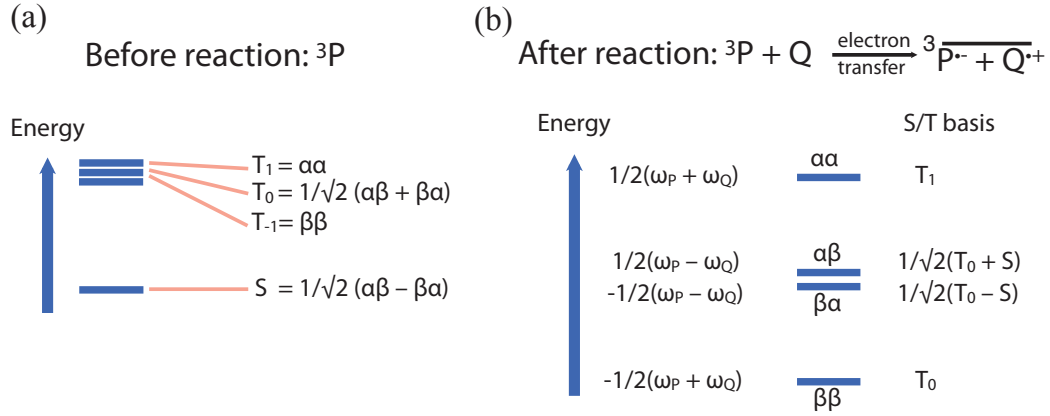
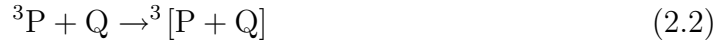


Figure 2.3: Energies in the singlet/triplet basis before (a) and after (b) reaction

radical pair, localized with a solvent shell,



In this pair, both species are radicals with parallel spins. This pair can now either diffuse apart in solution and react with other molecules (Equation 2.3) or it can recombine within the solvent cage, to reform the original species (Equation 2.5). If the geminate pair separates and reacts with other species then no nuclear polarization is generated. The other possible fate, recombination, is favored when the radicals have antiparallel electron spins. In this case they reform to generate a low energy ground state singlet.



Thus, the triplet geminate pair must first convert to a singlet state, via electron spin-flips. Before reaction, the triplet energy states in P are far removed from the singlet state (Figure 2.3(a)). However, once the geminate pair is formed, the electrons are far removed from each other, mixing the energies of the S and T_0 states (Figure

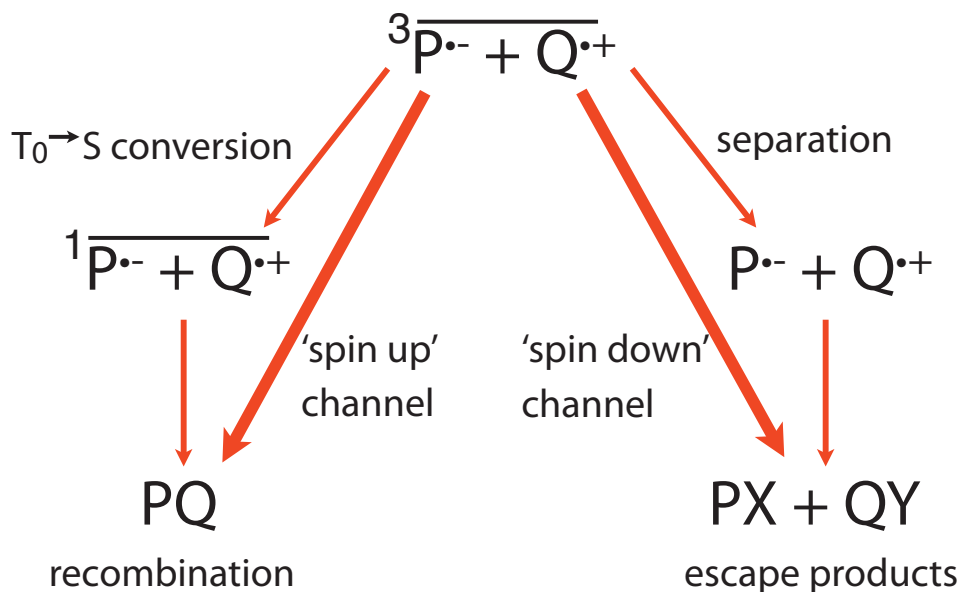


Figure 2.4: Radical pair mechanism summary

2.3(b)). The $T \rightarrow S$ conversion rate is given by the difference in EPR frequencies of the two electrons in the geminate pair. This means that any factor that affects the EPR frequencies of the electrons will have a direct affect on the products of the reaction; driving it either towards recombination or separation.

The magnitude of the difference in the two EPR frequencies in the geminate pair is in general much smaller than the magnitude of a single EPR frequency. Hence, the $T \rightarrow S$ conversion rate can be affected by relatively small perturbations in the EPR frequency. The perturbation relevant to photo-CIDNP is the electron-nuclear hyperfine coupling. Depending on the value of the hyperfine coupling, the $T \rightarrow S$ conversion rate will either be increased or decreased if the nuclei are spin up or down. The result of this interaction is that the products of the recombination path will be enriched in the nuclear spin which increased the $T \rightarrow S$ conversion rate. The products of separation will be enriched in the nuclear spin which decreased the $T \rightarrow S$ rate. The "spin sorting" nature of the the radical pair mechanism is summarized in Figure(2.4).

In systems where the recombination products are the same as the separation products, the radical pair mechanism, as it stands, will give no polarization enhancement as no net polarization is generated. However, this model does not take into account nuclear spin relaxation. Spin-lattice relaxation is fast for nuclei in species with para-

magnetic electrons, such as radicals. Thus, for the longer-lived radical species that do not undergo quick recombination, nuclear polarization is reduced. The nuclei in the species that undergo quick recombination maintain polarization for much longer. The result is a small overall net polarization in the solution.

As a footnote, the radical pair mechanism is of a wider importance than just as an explanation for the CIDNP effect. It is the most common mechanism behind magnetic field effects (MFEs) in chemical reactions, whereby the application of a magnetic field can have a profound effect to upon the product ratio [6]. One particularly fascinating case of an MFE is in avian magnetoreception [51]. Recently results have fueled the suspicion that birds navigate by monitoring a photo-initiated chemical reaction whose product ratio is a function of the orientation of the Earth's field. Whilst the exact chemistry is not known, experiments have shown that such a mechanism is feasible [41].

2.2.3 Experimental

Initially we attempted to observe the photo-CIDNP effect by using a 1.3 W 532 nm continuous wave green laser (OEM Laser Systems) to excite a solution of flavin mononucleotide (FMN) and N-acetyl tryptophan (TrpH). FMN is probably the most commonly used chromophore for photo-CIDNP experiments, forming a very intense green/yellow solution. The laser was coupled to the solution sample in the magnet by the use of an optical fiber (Newport). Despite many attempts, there was no CIDNP enhancement observed during these experiments.

In all previous known experiments, photo-excitation for the FMN has been provided by a multi-line mode Ar-ion laser, delivering light principally at wavelengths 488 nm and 514 nm. There is some evidence that it is the 488 nm line that excites the FMN into the excited triplet. Absorption at 514 nm is weaker and may not lead to the desired triplet state [30]. Thus, excitation at 532 nm may be very inefficient. Furthermore, there was significant sample heating observed during the laser pulse which led to line broadening and possibly obscured any small CIDNP enhancement.

Fortunately the lab was also equipped with a XeCl excimer laser. The principal output of this laser is in the UV, at 308 nm. Whilst this is not appropriate for excitation of FMN, a different molecule - 2,2'-dipyridyl (DP) - has been studied in depth [63] [64] [65] for its properties as a photoCIDNP agent absorbing at this frequency and it was decided that we should use this instead of FMN.

DP shows strong photo-CIDNP polarization enhancements in photo-initiated reactions with tryptophan, tyrosine and histidine. For this experiment we decided to continue with the reaction between our photosensitizer and TrpH. This is a cyclic process, as described in the previous section, where the products are the same as the

reactants. The advantage of such a system is that the CIDNP experiment can be run repeatedly on the same sample where it should give the same signal enhancement every time, all else being equal. In reality this is not quite true, and there is some leakage of reactants with every laser pulse. The dye gradually photobleaches with each pulse either through oxidation of the excited triplet state or through photoreduction. Conolly and Hoch [13] reported that increasing oxygen concentration in solution improves the size of the CIDNP enhancement when using FMN as a photosensitizer due to the photoreduced FMN being reoxidized by the O_2 in solution. However, high concentrations of O_2 are found to efficiently quench the photoexcited triplet, so there is an optimal O_2 concentration for the FMN-amino acid system. Fewer studies have been carried out on the DP-amino acid system and in general most experiments on this system begin with degassing of the solution. We found that the CIDNP signal was optimized by minimizing the concentration of O_2 in solution.

DP and TrpH were obtained in the highest available purity from Sigma Aldrich and used without further purification. 99.99 % D_2O was purchased from Cambridge Isotope Laboratory (CIL). The experiments were conducted on solutions of around 0.5 mmol of DP and 3 mmol of TrpH. The solutions were purged of O_2 by bubbling with N_2 for 30 minutes before each experiment. This process increased the photoCIDNP signal by a factor of two compared with a normal oxygenated sample.

The method of coupling the laser light to the solution is shown in Figure 2.5, in a similar manner to that shown previously by Pienta and Smith [50]. A XeCl (308 nm) MPB Communications excimer laser was used for sample illumination, triggered by transistor-transistor logic (TTL) pulses. Its peak pulse energy was approximately 100 mJ, with a pulse duration of 5 ns. Coupling of laser light to the NMR probe was achieved by focusing the output UV light onto the end of a 7 mm diameter liquid light guide. The 79 inch light guide was long enough such that the laser could be placed outside the 5 Gauss line of the magnet and the sample inserted into the magnet from above. The magnetic susceptibility mismatch between the metallic sheath of the light guide and the solution necessitated the addition of a 1 inch length of quartz rod butted up against the output of the light guide. The mask was applied to the end of the quartz rod using a UV-absorbing ink (Figure 2.5(b)). The tip of the rod was then dipped in the DP and TrpH solution. Losses of around 95 % of light over the path from laser output to sample were recorded. It was found to be crucial to regularly change the gas used as the lasing medium. The preliminary experiments run using the laser showed no CIDNP polarization whatsoever, even though the laser appeared to be running normally. Only upon changing the XeCl gas did the CIDNP signal appear.

The photoCIDNP imaging experiments were carried out on a 300 MHz (7.04 T) Bruker Avance 300 spectrometer with a 10 mm Bruker microimaging probe and gradient stack. Images were obtained using a modified Bruker CSI sequence [8] (Figure

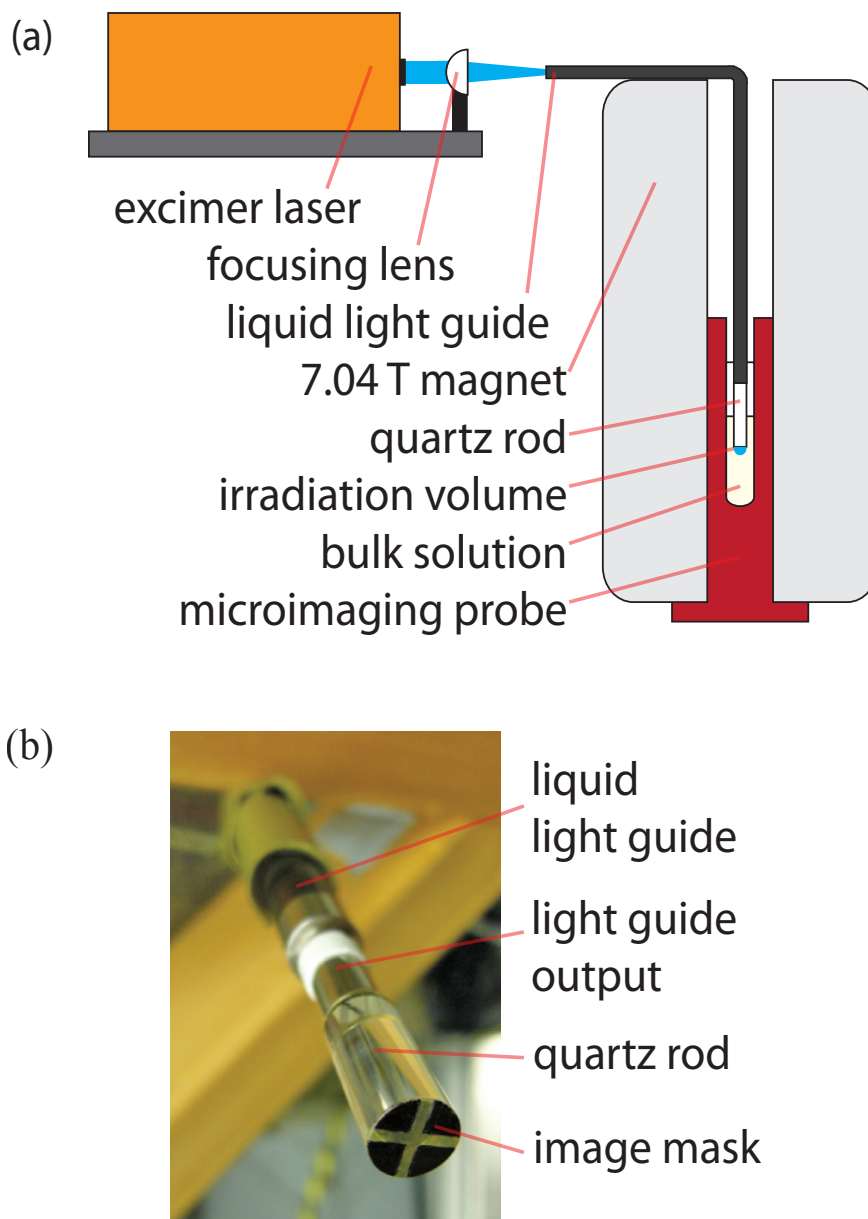


Figure 2.5: (a) Experimental apparatus (b) Output of light guide.

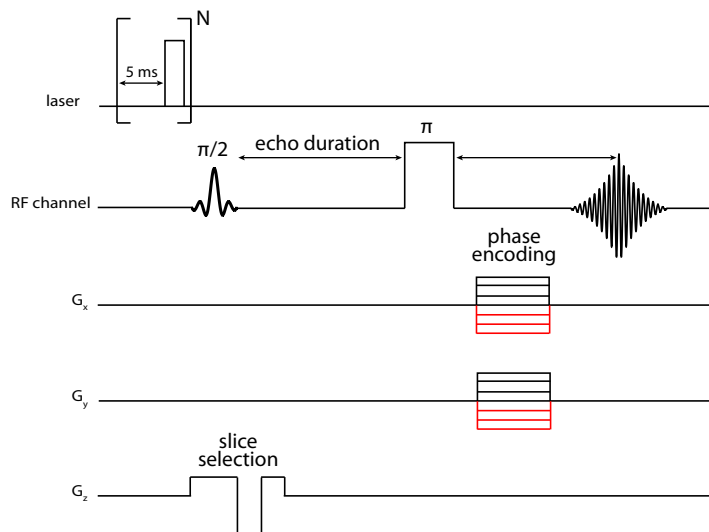


Figure 2.6: Modified CSI sequence (omitting presaturation and water suppression pulses). For laser pulse-train experiments, $N=50$. For ultra-fast optical encoding experiments, $N=1$.

2.6). A spin echo sequence was used to excite a particular slice of the sample. Following the refocusing 180 degree pulse, phase encoding gradients were applied in two dimensions. The FID was then recorded in the absence of gradients acquiring a spectroscopic signal. The spatial information for the spins was encoded into the phase of the nuclear spins. The inbuilt Bruker CSI sequence was modified slightly by the addition of a single laser pulse or a train of laser pulses directly before the excitation.

Before recording an image, spectra were taken in order to directly observe the photo-CIDNP polarization. The polarization enhancement shown in (Figure 2.7(b)) was obtained following a pulse train of 50 laser pulses over a period of 500 msec. As can be seen from the spectrum, the photoCIDNP enhancement was greatest for the 3,4 and 5 positions of DP. Thus the region between 7.5 and 9.0 ppm was selected for the CSI images in order to minimize the effect of any residual thermal polarization of the unenhanced protons. By direct comparison with area under the DP peaks in the thermal spectrum, we estimate the photo-CIDNP enhancement for the whole volume to be about a factor of fifty. However, the photo-CIDNP enhancement was not isotropic across the volume of the RF coil. The laser light was absorbed as it passed through solution, meaning that the majority of the polarization enhancement

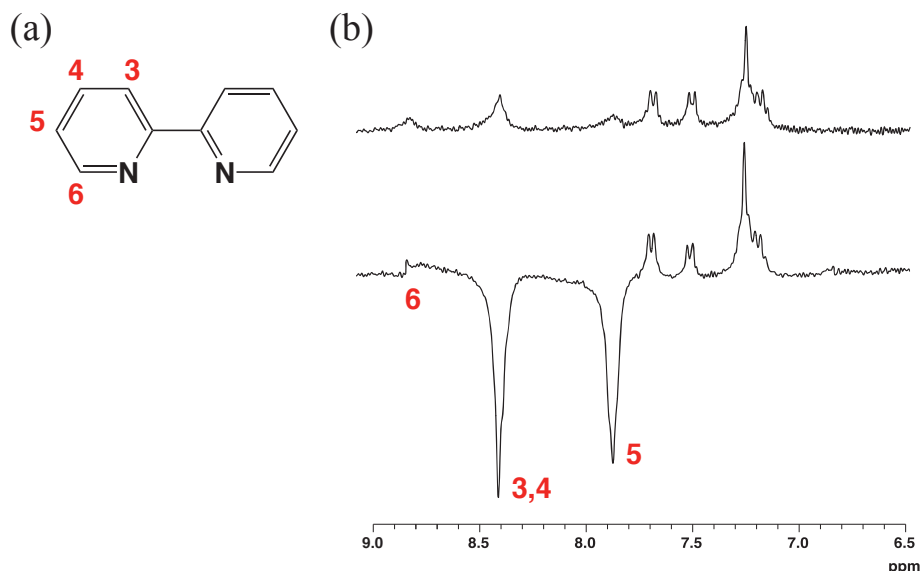


Figure 2.7: (a) Structure of DP (b) Dark spectrum *vs* photo-CIDNP spectrum

was in the region closest to the light guide.

2.2.4 Results

To maximize signal initially the imaging experiments were run using a train of laser pulses in order to build up high levels of polarization before the excitation 90 pulse (a pseudo steady state experiment [24]). However, whilst this is sufficient to show that optical spatial encoding is possible, it is not "ultra-fast" encoding due to the laser pulse train lasting hundreds of milliseconds.

In order to ascertain the depth of penetration of laser light into the sample, a coronally-orientated CSI image was taken. A Tripilot imaging sequence was used to acquire the "guide" images (Figure 2.8(a)). This left a cross-shaped artifact on the image due to the rapid acquisition of slices in 3 dimensions. It is unfortunate that this resembles the eventual cross-shaped ultrafast image. The cross artifact is absent from all CSI images as only one slice was selected for these experiments. From the coronal image (Figure 2.8(b)) it was estimated that the vast majority of the photo-CIDNP enhancement was in the first millimeter directly below the light guide. Correcting for the difference in volume between the entire RF coil and the excited region, the polarization enhancement in the excited region was a factor of 500 or greater. The UV

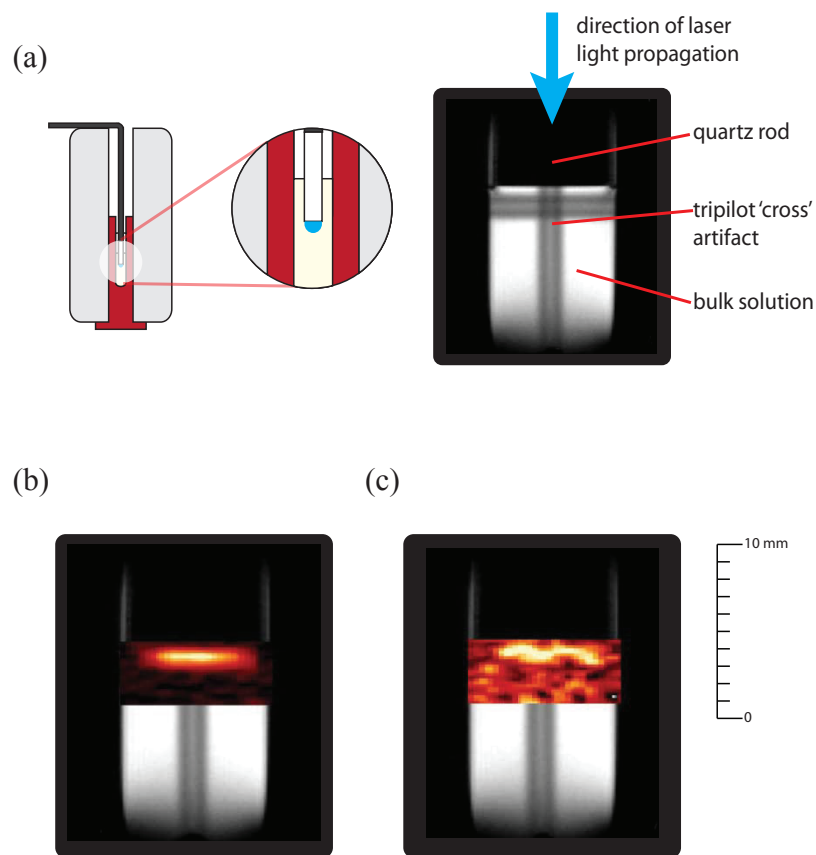


Figure 2.8: Coronal images (a) Tripilot guide image of H_2O in solution (b) Guide image with overlaid laser pulse-train photo-CIDNP CSI image. Note the formation of polarization in the region immediately below the quartz rod (c) Single laser-pulse ultra-fast optically encoded image.

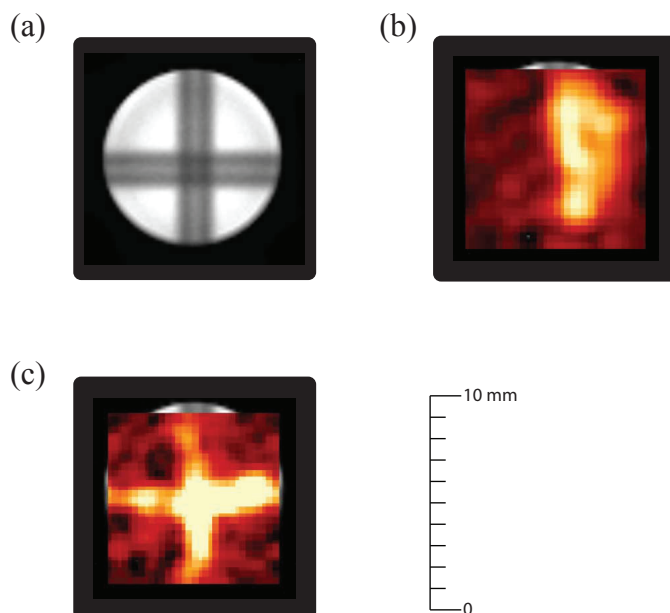


Figure 2.9: Axial images (a) Tripilot guide image, again showing artifact (b) Guide image with overlaid laser pulse-train photo-CIDNP CSI image, semicircle shape (c) Guide image with overlaid laser pulse-train photo-CIDNP CSI image, cross-shape

laser light penetrates about 1 mm into the bulk sample before significant attenuation, so a 1 mm thin slice immediately below the light guide was selected for axial imaging.

Half of the quartz rod was obscured with ink and an axial image was acquired (Figure 2.9 (b)). A semicircular enhanced region is clearly visible. A negative of a cross was then marked on the end of the quartz rod and a further image was acquired (Figure 2.9 (c)).

Having obtained good results running the experiments with a laser pulse train, we moved to single laser pulse excitations in order to show true ultrafast optical encoding.

The polarization generated following a single laser pulse was roughly equal to the thermal polarization. The problem of comparatively low polarization was compounded by the presence of a large water peak and broadening of the CIDNP resonances due to heating and inhomogeneity on the light guide/solution interface. Fortunately the Bruker Paravision interface allows for easy inclusion of water suppression, using the VAPOR sequence [60], and presaturation in order to remove all thermally polarized signal. Even with these elements in place, the low signal necessitated the

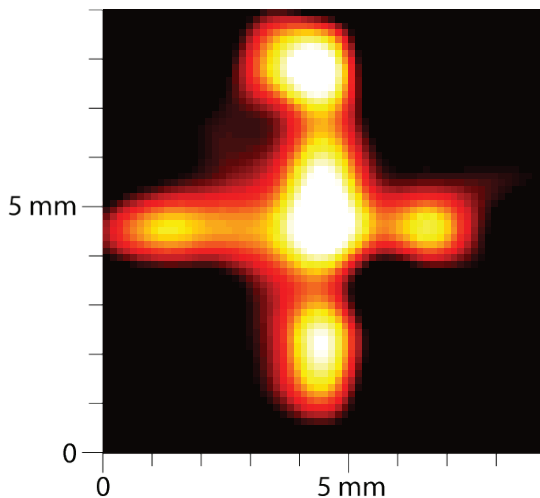


Figure 2.10: Single laser pulse ultra-fast optically-encoded image. 9×9 resolution. \times

collection of 200 transients per voxel. The image resolution was somewhat limited by the large susceptibility gradient in the area being imaged, in this case directly on the interface between the quartz glass and the aqueous solution.

A coronal image was taken initially, showing a small CIDNP enhancement in the region directly below the quartz rod, as before (Figure 2.8(c)). The signal from a coronally-oriented experiment is intrinsically higher in this experiment than from an axially-oriented experiment. This is because, axially, each voxel is only 1 mm deep where coronally, the center voxel are the sum of signal across the full diameter of the NMR tube; 10 mm. The axial image, again of a cross, proved harder to obtain. However, following optimization of the NMR pulses and experimental conditions, an ultra-fast optically encoded image was acquired (Figure 2.10).

2.2.5 Discussion

The optical encoding time in this experiment is given by the time taken for CIDNP polarization to develop following laser excitation of the photosensitizing agent. Previous time-resolved CIDNP experiments [63] [64] [65] have shown this to be in the sub-microsecond timescale. The limitations of RF power, requiring excitation pulses in the microsecond range, make it very difficult to study the evolution of NMR magnetization on a faster timescale. Thus, the optical encoding time may be faster still.

Our experiments demonstrate that the time required to encode an MRI image

can be significantly reduced by manipulating optical transitions that are coupled to spin degrees of freedom, in this case through the photoCIDNP effect. The experiment in its current form may be productively applied to the study of fast protein folding in combination with remotely detected NMR in microfluidic devices or for studying turbulent and dispersive flow at time scales currently inaccessible to MRI. Next, while we have acquired a conventional image to demonstrate the successful spatial encoding of spins, our method in principle can be extended to obviate the need for gradients all together. In this case, the image can be reconstructed by a point-by-point acquisition, either directly or using chemical exchange or diffusion to yield a large signal enhancement [12]; the sensitivity of the approach will improve dramatically as the voxel dimensions are reduced. Further, because there are numerous technologies to generate a desired spatial pattern of optical irradiation, either by scanning or masking, our method can also be used in a Fourier mode to generate an image of spins in the sample without magnetic field gradients, an example of single pixel imaging [19]. In this case, the resolution might be improved by by a two-photon excitation scheme, yielding photo-CIDNP excitation only in the region of interaction between multiple laser pulses. More speculatively, approaches based on optical excitation in triplet-forming solutes or in solids [66] may join recently proposed schemes for nanoscale optical detection of MRI [5] [15], in which case the optical excitation of the sample or an optically active substrate on which the sample has been deposited may be used for spatial encoding of all-optical MRI experiments.

2.3 Spatial Encoding Using Localized Permanent Magnets

High throughput screening (HTS) has become a workhorse method in the chemical and biological industries, particularly in the field of drug discovery. HTS consists of a series of parallel assays run on a single plate, each plate dotted with wells. Each individual well is the site of a particular assay, screening the molecule of interest against a particular chemical compound. More recent advances in the field have shown that the process can be speeded up significantly by moving away from wells and running the assays in microfluidic channels [20].

To date, most detection methods used for microfluidic experiments have been optical, requiring a fluorescent dye or tracer. There are some serious disadvantages to using this detection mode; foreign compounds must be added to the assay and optical methods are inherently incapable of studying reactions in opaque materials. NMR offers to HTS the advantages of high spectroscopic resolution and the possibility of MRI of microfluidic chips. However, due to the very poor filling factor of a microfluidic channel in an NMR probe, conventional NMR is too insensitive to be

used. One solution is to build individual micro-detection and excitation coils for each individual channel used [43]. In systems with up to 100 or more channels, the drawback of crosstalk between channels and the complexity of the RF circuitry makes this approach unappealing.

Applying remote detection methodology, pioneered in this lab [55] [44] mitigates this problem to an extent, allowing us to encode magnetic information on the chip using a single RF excitation coil and then detect in a single dedicated remote detection coil. Ultimately the size of the linear gradient that can be applied in the spatial encoding step limits the resolution, and thus the number of channels that can be individually addressed in the remote experiment.

Given the fact that pulsed magnetic field gradients require cumbersome electronics and are power-hungry, it would be advantageous to dispense with them altogether if possible. This would significantly cheapen the technology, bringing us closer to a commercially available high-throughput NMR assaying device. As just shown, photo-CIDNP could be used, though this reintroduces many of the problems of using optically-detected fluorescence.

Application of permanent magnets directly to the microfluidic channels themselves supplants the need for pulsed field gradients. By controlling the size of the field from different regions of permanent magnets either through modifying the layer thickness or differing magnetic material, spatial information can be encoded onto the spins, in much the same way as a gradient in a conventional MRI experiment. Thus, for example, if channel 1 is coated with material A and channel 2 with material B, then the spins will feel different field strengths depending on the material coating the channel. The differing Larmor frequency in these regions can be converted into a phase difference and read out in the detection coil.

In its simplest form, this technique allows us to independently encode as many channels as we have different materials or layer thicknesses. However, in a microfluidic chip, fluid is flowing, opening up a second dimension for our encoding. For each channel we can create regions of different field strengths. A given plug of liquid flowing through the channel will sequentially experience a series of different field strengths. The residence time in each region will be a function of the linear flow velocity and the size of each region. By applying a train of frequency selective pulses tailored to a given series of different field regions, we can select a given channel with high specificity, analogous to reading a barcode.

Its interesting to note that this technique is not possible using conventional pulsed field gradients as the field gradient generated is inherently linear. Using this technique we can generate an arbitrarily high apparent “gradient”.

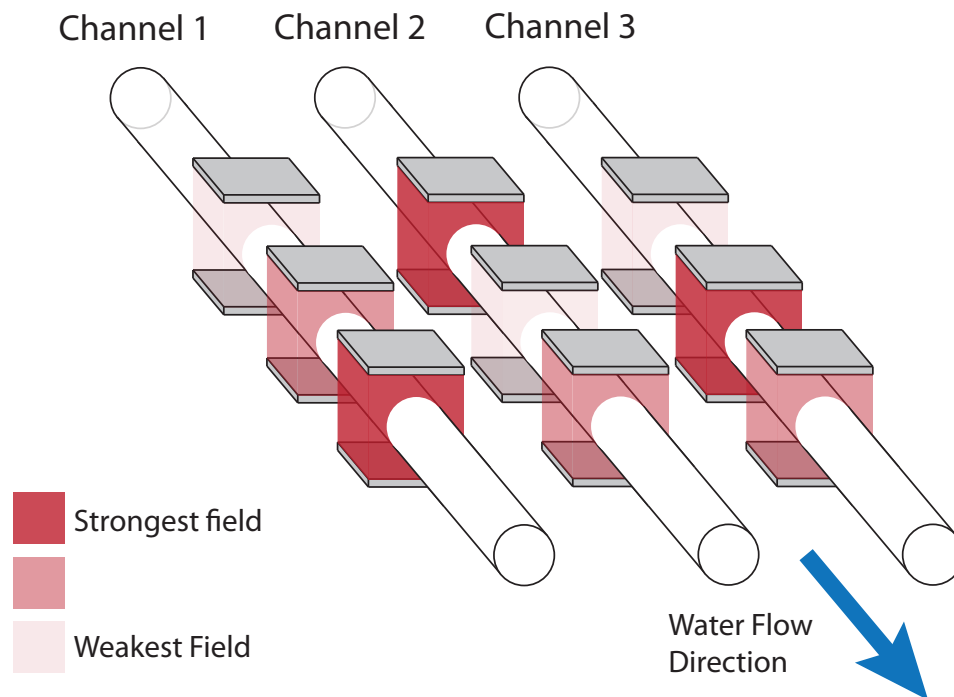


Figure 2.11: Example "barcode" marking of microfluidic channels, using regions of differing field strength

2.3.1 Local Field Encoding Results

Microfabrication of the magnetic nanostructures required for this experiment, whilst rather straightforward in skilled hands, requires experience obtained over months of training. As a proof of principle experiment, it is sufficient to show the ability to selectively excite a particular plug of water based only on the frequency “barcode” created by permanent magnets of varying strength placed along the course of the channel, without microfabrication.

In order to select the correct material for the field encoding, there are two main criteria: control over field strength and field homogeneity.

Frequency selection would theoretically be made easier by applying stronger magnetic fields; the different encoding regions would then be very well separated in frequency. However, strong permanent magnets can cause serious problems with inhomogeneity of the magnetic field, and if the field is too strong, the Larmor frequency of the protons could be shifted out of the tuning range of the probe altogether. Thus the shift in Larmor frequency caused by the magnetic structures needs to be tailored to be as small as possible, given the limitation that too small a shift will make frequency selection difficult.

As suggested earlier, one way to control field strength is to simply use different materials. A subtler way is to use powdered magnetic material mixed with a non-magnetic material, such as epoxy resin, changing the concentration of magnetic powder in order to tune the field strength. Field strength can also be controlled by changing the volume of the magnetic material or changing the distance of the magnetic material from the volume being studied.

In order to generate a homogeneous magnetic field, one optimal solution is to have a thin magnetic plate above and below the volume of interest. In this mode, the thinner the plates, the better the homogeneity. The field strength between the plates is then simply a function of the thickness of the applied magnetic layers.

As this experiment was run on a high-field magnet, we could use either diamagnets, creating an area of reduced field strength between the plates or paramagnets, creating an area of increased field strength between the plates. Whilst a number of metals have desirable magnetic properties, the skin-depth effect, whereby conductive materials absorb high-frequency electromagnetic radiation, precludes their use. The skin depth, δ of a material is given by

$$\delta = \sqrt{\frac{2\rho}{\omega\mu}} \quad (2.6)$$

where ρ is the resistivity of the material, ω is the frequency of the radiation and μ is

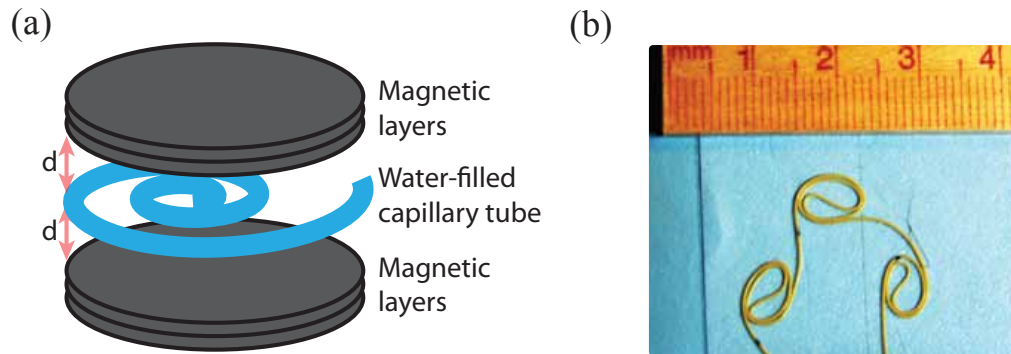


Figure 2.12: (a) "Sandwich" of magnetic layers (b) Coiled capillary tubing affixed to masking tape, before casting in epoxy resin

the magnetic permeability of the conductor.

Bismuth, for example, is appropriately diamagnetic with a magnetic susceptibility of -3.55×10^{-9} but a layer thicker than 2 microns almost completely shields 300 MHz radiofrequency radiation.

Magnetic storage media such as high-density floppy disks consist of a layer of mylar sandwiched between a pair of 1 micron layers of cobalt-ferric oxide CoFe_2O_4 [47]. These are ideal thin-layer magnets for the purpose of generating a small homogeneous field. To determine the size of the frequency shift imparted by the disks, a water-filled microfluidic chip phantom was sandwiched between two layers of floppy disk (Figure 2.12)(a). The phantom was designed such that it was possible to move the magnetic layers apart in order to control the size of the applied frequency shift.

Rather than having a chip custom-built for us, it was decided to make a phantom out of coiled capillary tubing. Upon initial construction it was realized that capillary tubing doesn't like to stay coiled for very long! Thus a method was developed to cast the capillary tubing in resin. The resultant chip is very robust. The steps for resin casting are given here such that future students can repeat it:

- 1) Lay down a layer of double-sided Scotch tape on a flat surface. On top of this attach a layer of masking tape, sticky side up.
- 2) Affix the capillary tubing to the layer of masking tape in the required pattern. The sticky layer should prevent it from uncoiling at the points of stress in the tubing.
- 3) Find a heavy flat-sided object and affix Teflon tape to a region of it the same size as the required phantom. Now coat the capillary tubing liberally in 2-part epoxy. This will immediately start to dissolve the glue, so as quickly as possible, lay the

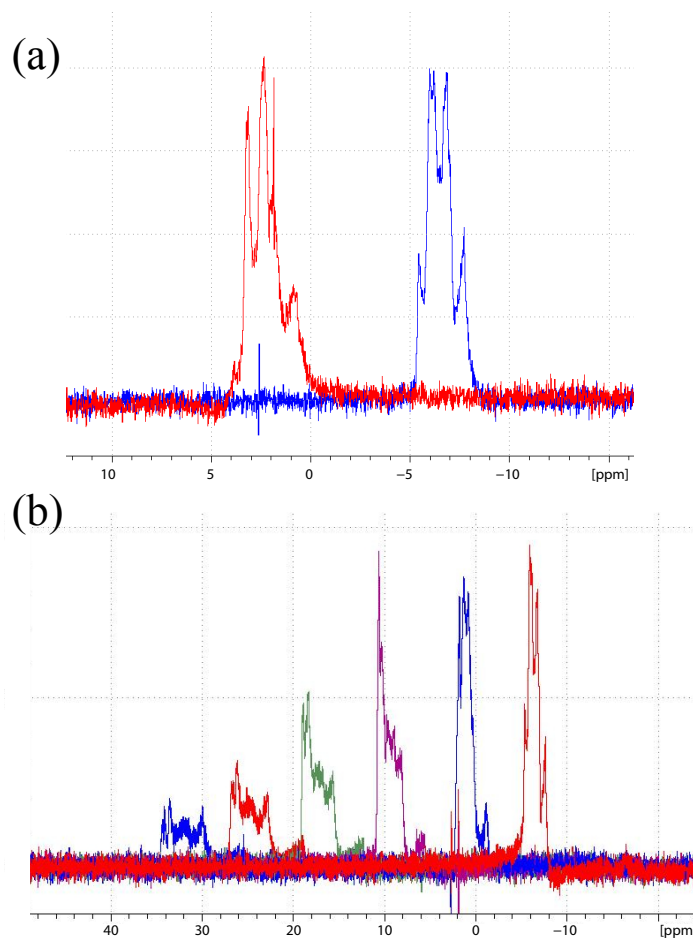


Figure 2.13: (a) Frequency shift on addition of 1 layer of magnetic disk, in close contact with capillary (b) Successive frequency shifts (right to left) on addition of successive layers of magnetic material.

heavy object on the capillary tubing so that the Teflon tape is in contact with it.

4) Leave to harden fully.

5) Carefully pull away the Teflon tape and masking tape. The capillary tubing will be cast in a thin layer of epoxy resin.

The shift in frequency when extra floppy disk layers were added was recorded using a 300 MHz (7.04 T) Bruker Avance 300 spectrometer with a 10 mm Bruker proton probe. Figure 2.13(a) shows the frequency shift upon addition of a single layer of magnetic material to each side of the capillary tube chip. The distance between the two sandwich layers, ($2d$ in Figure 2.12(a)), was 500 microns. The shift in frequency is roughly 10 ppm (3 kHz). Figure 2.13(b) shows the Larmor frequency of the water in the chip upon addition of successive layers to each side. The separation between layers in this case was about 1.8 mm. The frequency shift per layer was about 8 ppm (2.4 kHz), though after addition of 5 layers, line broadening was in the region of 2 kHz.

The significant change in precession frequency in both cases is enough to allow for selective pulses to single out different regions for specific excitation. One concern for these experiments was the possibility of significant line broadening due to inhomogeneities introduced by the magnetic material. Whilst there is some broadening of the resonances, particularly with extra layers, it is within the acceptable limit for a selective pulse.

This proof of principle experiment has shown that it is possible to control the magnetic field locally, using applied magnets. This control can be achieved either through changing the separation of the magnetic plates, or modifying their thickness. The next step is to show that in a flowing chip, the pattern of applied magnets can be used to selectively excite a given channel. These experiments are ongoing in the lab.

Chapter 3

Xe Relaxation Studies

As was outlined in Chapter 1, the thermal polarization of nuclear spins at room temperature is poor. The most common nucleus in the body, the proton (^1H) is fortunately also the easiest to study in an MRI experiment, but not all organs in the body contain a high proton density. Particularly significant is the lung, which simply shows up as a void in an MRI scanner. In order to view this void space a gas could be used, but the low density combined with low polarization renders thermally polarized gases essentially invisible. This fact has provided a driving force for research into noble gas hyperpolarization. Through spin-exchange optical pumping, polarization of Xe or He can exceed 50 %, rendering an enhancement in lung signals of four or five orders of magnitude. Although still very much in the realms of research medicine, hyperpolarization has enabled scientists to take detailed images of organs like the lungs and sinuses. At high magnetic fields this leads to a significant increase in MRI signal. At low magnetic fields this effect is even more pronounced, as the thermal polarization is comparatively much smaller [56].

It was decided to test the viability of gas-phase NMR imaging using a single sided NMR magnet, where the homogenous region lies outside of the magnet itself. Such a device could find use in a doctors surgery or for point-of-care medical professionals. One particularly interesting application for a cheap, portable gas-phase MRI device would be for diagnosis of respiratory diseases. In regions where there isn't the funding to buy an expensive high-field clinical scanner, a cheap alternative could be a life-saver. Commercialization of such a system would be contingent upon the parallel development of a cheap, portable Xe hyperpolarization device, but steps are also being taken in this direction [58].

In the series of experiments described in this chapter we did not ultimately manage to obtain a gas phase ex-situ Xe image, the reasons for which I will outline. Nonetheless we obtained a very interesting result in the observation of a startlingly long T_2 ;

one of the longest liquid state T_2 decay times recorded. Furthermore, following this experiment, we decided to study the transverse relaxation in more detail, this time at high magnetic field. I hope that the experimental details described in this chapter are of relevance to future Xe studies which will be carried out in this lab, whether in generating liquid Xe for ultra-high polarization experiments or developing low-field Xe excitation and detection electronics.

3.1 Ex-Situ NMR

A major research thrust of this lab is ex-situ NMR. This has been covered in great depth in the Ph.D. dissertations of Frank [21], Paulsen [49], and Demas [16], amongst others, and I refer the reader to this work for further information. Here I shall just give a perfunctory introduction, sufficient for the understanding of the proceeding sections.

NMR and MRI are characterized by their reliance on huge expensive magnets requiring costly cryogenics to run and upkeep. However, in theory, NMR need not require such engineering marvels. They exist mainly to create high magnetic fields, such that equilibrium polarization is maximized and to generate very homogeneous magnetic fields, where homogeneity is measured in parts per billion. As we have seen, high polarizations can be achieved through other means. Does this mean, then, that if we can generate very stable homogeneous low magnetic fields we can render the high-field magnet obsolete? Well — not quite — the very high gyromagnetic ratio and chemical shift are crucial to experiments in solid-state NMR and protein spectroscopy, amongst others. Nevertheless, much of what is done at high field, particularly in MRI, could in theory be done at low magnetic field, if only we could make the magnets to do it.

Previously unaddressable problems become approachable once one lifts the constraint of requiring a large superconducting coil. One can run NMR outside of the magnet, using single-sided permanent magnets whose sweet spot lies outside of the body of the device. These ex-situ magnets have applications in point-of-care medical diagnostics and for running experiments on samples too large to fit into a high-field NMR magnet. This work was pioneered by Jackson in his use of inside-out magnets for oil-well logging and more recently has been commercialized in the form Prof Bernhard Blumich's NMR Mouse.

One such single sided NMR device was designed and constructed by Dr Jeff Paulsen and was used for the following experiments. This magnet consists of 4 rotatable cylindrical $\text{Nd}_2\text{Fe}_{14}\text{B}$ magnetic dipoles. The sweet spot with highest field homogeneity lies about 5 cm from the magnet surface, though this distance can be

adjusted by rotation of the dipoles. An exhaustive description can be found in Dr Paulsen’s Ph.D. dissertation [49].

3.2 Xe Hyperpolarization

Hyperpolarization of Xe gas for this experiment was achieved using a Xe polarizer constructed in-house, in the large part by the efforts of Rhys Garmann and Dr Xin Zhou. A mixture of Xe, He and N₂ is flowed into a transparent glass cell. The cell is heated to approximately 150 C in order to vaporize a small quantity of metallic Rb also present in the cell. Four 795 nm diode lasers, with a total output of 150 W are directed into the cell. The laser light is circularly polarized, exciting the Rb 5²S to 5²P transition specifically for electrons of a particular spin orientation when in a leading magnetic field. Spin-retention during relaxation from ²P back to ²S leads to a build up of electron spin polarization under conditions of continuous laser irradiation. Short-lived van der Waals complexes formed upon collisions between Xe and Rb allow transfer of spin polarization via the electron-nuclear hyperfine coupling. Nuclear polarization built-up on Xe persists due to the long T_1 of Xe, allowing the relatively slow spin-exchange process to create large ensemble polarizations of Xe. The polarizer used for these experiments outputted a Xe polarization of about 5 %.

The raw gas mixture outputted from the Xe polarizer is mainly composed of He and N₂. For the experiments with gas-phase Xe it was important to obtain the maximum possible signal, so pure hyperpolarized Xe was required. In order to achieve this the Xe polarizer was run in batch mode, whereby the Xe was condensed out of the output gas mixture in a cold finger, letting the more volatile gases, He and N₂, flow out of the system. In order to maintain polarization during the duration of collection, the cold finger was placed in a leading field of 0.5 T. Batch-mode collection times varied from 15 to 45 minutes depending on the experiment.

3.3 Low-Field Xe Probe Design

Previous experiments using the ex-situ magnet were run solely for the detection of proton NMR. Xe detection necessitated the construction of new RF electronics, reflecting the fact that γ_{Xe} is only about 1/4 of that of the proton. For an experiment to be considered truly single-sided, the sample should not only lie outside of the body of the magnet — it should lie outside of the RF coil as well. The applications of a single sided magnet for medicine or in-the-field diagnostics are significantly reduced if the sample needs to be manhandled into the middle of a solenoid or saddle coil. Thus, a surface coil was used for the Xe probe, consisting of a length of copper wire

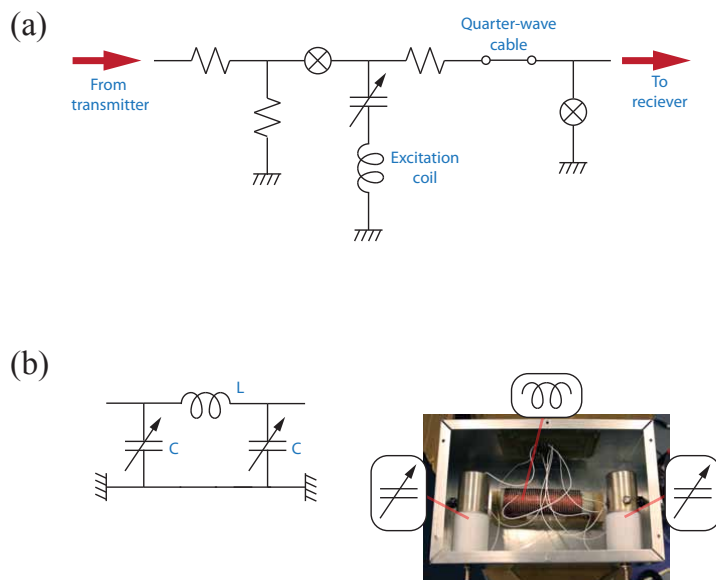


Figure 3.1: (a) Duplexer circuitry (b) Pi circuit required at low frequency

wound into a flat coil.

Before continuing, its worth mentioning that general probe and spectrometer design is covered in depth in *Experimental Pulse NMR A Nuts and Bolts Approach* by Fukushima [22], and the interested reader is directed there for more information.

In the sweet spot of the magnet, the field strength is about 260 Gauss. At this field the Larmor frequency of Xe is about 610 kHz. The RF circuitry at this low Larmor frequency is slightly different from the corresponding circuitry at high field.

An Apollo LF Spectrometer (Tecmag) was used as a transmitter and receiver. The RF waveform was amplified using a CPC MRI Plus RF amplifier. The RF current then passed through a duplexer. The role of a duplexer is to prevent the high-power excitation current passing straight through to the sensitive receiver circuitry, potentially damaging it. The duplexer which was already present, used for proton excitation at a Larmor frequency of 2.205 MHz, needed redesign for the lower RF excitation frequency of 610 kHz. The duplexer was constructed as shown in Figure 3.1(a). The crossed diodes act as an amplitude high-pass filter: they are closed for high-power RF and open for low-power RF. When the transmitter is active, both diodes act as closed switches. Downstream from the quarter wave cable there is essentially zero impedance, so the quarter-wave cable acts as an open circuit. All the

transmitter energy is directed into the excitation coil. When the transmitter is off, the diodes act as open switches and any noise is directed straight to ground.

When the excitation coil is acting as a receiver, the current is low, so the diodes again appear as open switches. In this case the circuit after the quarter wave cable no longer has zero impedance, and acts as closed, so the current flows to the receiver.

The fly in the ointment here is that at 610 kHz the length of a quarter-wave cable is about 75 m. Excluding the fact that a length of cable this long will be the source of a large quantity of noise, it is also simply not practical. A simple replacement to a quarter wave cable at low frequencies is a pi-circuit (Figure 3.1(b)) so called due to its π -shape. Constructed properly, the pi circuit should behave in exactly the same way as a quarter wave cable.

Tuning and matching of the transmitter/receiver coil was carried out as standard, using two variable capacitors. Due to the low frequency, the required capacitances are high, necessitating the use of rather large (approx. 10 cm long) variable capacitors.

Generation of batch-mode Xe is a rather time-consuming process and we thus decided to calibrate the 90 degree pulse time using a sample of ^{13}C enriched organic solid instead. The 90 acquired from this experiment (50 microseconds) is likely to be a little shorter than that of Xe, whose gyromagnetic ratio of $73.997 \text{ rads}^{-1}\text{T}^{-1}$ is slightly higher than that of ^{13}C , $67.283 \text{ rads}^{-1}\text{T}^{-1}$.

3.4 Low-Field Gas-Phase Xe Experiments

Before running an imaging experiment it was decided to first observe the bulk gaseous Xe signal. We used a Carr-Purcell-Meiboom-Gill (CPMG) sequence to maximize the observed signal. This sequence is essentially a train of Hahn echoes, the phase of each echo being cycled in order to correct more efficiently for off-resonance effects. In an inhomogeneous field such as this, a significant proportion of spins are off-resonant with the applied pulse, resulting in incomplete 180 nutations. If the phase of the 180 pulse is not modulated, the effect of each incomplete 180 pulse compounds on the previous.

Initially, observation of the direct output from the polarizer was attempted. The gas was flowed into a 5 cm diameter bulb placed in the sweet spot of the single-sided magnet. However, at 5 % abundance, the HP Xe signal is still small, and no Xe was observed. Subsequently, pure Xe was collected in batch-mode in the cold finger and then vaporized into the bulb. Pressures of up to 70 psi of pure HP Xe were achieved. However, even under these conditions, no Xe signal was observed.

The failure to observe gas-phase HP Xe was hypothesized to be largely due to

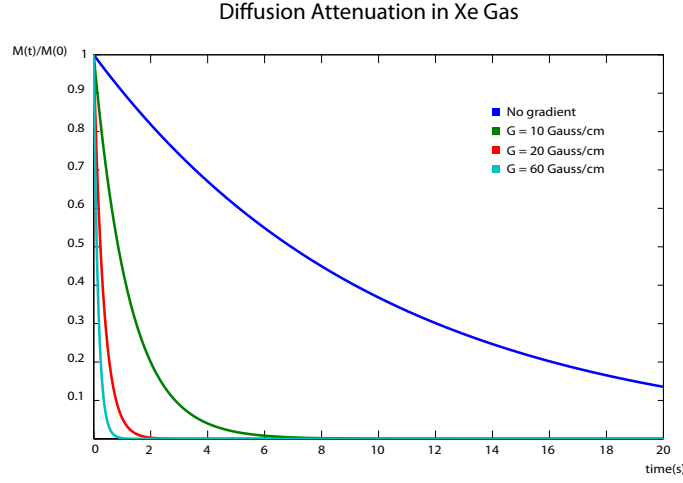


Figure 3.2: Diffusion attenuation enhanced T_2 in Xe gas, in different field gradients

the size of the inhomogeneity in the single-sided magnet. In conditions of fast diffusion, the CPMG echo train will only partially refocus the dephasing caused by an inhomogeneous magnetic field. The Hahn echo only perfectly refocuses in the limit of static nuclear spins. If there is significant displacement of spins across an inhomogeneous field in the period between echo pulses, then the refocusing will be incomplete. Following the 180 pulse, the spin essentially refocuses under a slightly different applied magnetic field from the under which it initially evolved. If the gradient is large enough, or the diffusion fast enough, the echo will not be formed at all.

Incorporating the effects of diffusion attenuation, the magnetization after a n echoes over a time, t , is given by [10]

$$\ln(M(t)/M(0)) = -\frac{t}{T_2} - \frac{\gamma^2 G^2 D t^3}{12n^3} \quad (3.1)$$

where D is the self-diffusion constant of Xe, γ is the gyromagnetic ratio, and G is the gradient in the magnetic field. The self-diffusion constant, D_{Xe} , is $0.061 \text{ cm}^2 \text{ s}^{-1}$ [11]. The T_2 of Xe gas was determined in this lab at high field in unpublished experiments and estimated to be around 10 s, though it is dependent both on wall coating and vessel size. In Figure 3.2 the T_2 envelopes for a CPMG sequence are shown given varying gradient sizes, assuming an echo duration of 1 msec.

For this magnet, G is not a well-defined quantity and differs across the bulb. From the field maps provided in Dr Paulsen's dissertation, it was initially estimated at 10 G/cm in the more inhomogeneous regions of the magnet and somewhat less in the

sweet spot. In this field gradient, the losses due to diffusion attenuation are small — about 1 % per echo. This being the case, diffusion attenuation alone cannot account for the lack of signal in the gas-phase Xe experiment. However, there is a lack of good information on the true size of the inhomogeneity of the field. If the gradient was closer to 60 or 70 G/cm, then this could be partly the cause of the lack of signal.

As well as transverse relaxation, longitudinal relaxation is also enhanced for gases in inhomogeneous magnetic fields [54]. Brownian motion in the presence of a field gradient causes the moving nuclei to experience a randomly fluctuating magnetic field. This has an effect very similar to the random field fluctuations caused by molecular motion in the liquid state; longitudinal relaxation. Typically, $\text{Xe}_{(g)}$ T_1 relaxation times are of the order of tens of minutes and can be ignored for experiments of short duration. However, inhomogeneously derived longitudinal relaxation is particularly pronounced when the magnetic field gradient is of the order of the size of the static field. Due to the distance between the polarizer and the magnet, the Xe atoms were undoubtedly flowing through a region of low field, perhaps as low as the Earth's field of half a Gauss. Given that they were then diffusing into a region of 260 Gauss, there was a significant field gradient. Thus, some of the polarization of Xe was undoubtedly lost on transfer. However, as we shall see in the following section, not all hyperpolarization can have been lost on transfer, as highly polarized liquid Xe was observed using this spectrometer.

As a footnote it is worth mentioning that similar problems were seen on attempting to detect hyperpolarized Xe gas using a vapor magnetometer at very low field by others in this lab. There is clearly some uncertainty about the spin dynamics of hyperpolarized gas at low field, an area which is probably deserving of more research.

3.5 Low-Field Liquid-Phase Experiments

Given the apparent inviability of detection of gas-phase Xe, it was decided to study the behavior of hyperpolarized liquid Xe at low field. For nuclear polarization density, few things come close to hyperpolarized liquid Xe: if your NMR system can't detect it, it's probably time to junk the system. This fact notwithstanding, the spin dynamics of concentrated hyperpolarized liquids are fascinating. At this level of polarization, the NMR signal is huge — there exist apocryphal stories of spectrometer receiver units being damaged by the sheer size of the induced current. Beyond the size of the signal, other effects such as radiation damping become significant and intermolecular quantum coherences become pronounced. It is observed, for example, that in highly polarized systems the T_2 becomes a function of the size of the flip angle of the spins [68].

3.5.1 Preparation of Liquid Xenon

At atmospheric pressure, Xe condenses to a liquid at 161.4 K, and freezes at 165.4 K. This implies a rather small temperature window in which to acquire liquid Xe. An acetone slush bath, at 178 K, is generally used for this purpose and seems quite adequate. However, its temperature is slightly higher than would be ideal and leads to incomplete condensation of vapor.

Liquid acetone was poured into a beaker. Ideally a dewar would have been used for this, but the small gap between NMR coil and sweet spot precluded using a vessel with thick walls. Gradually liquid N₂ was poured into the beaker with stirring, until a significant quantity of solid acetone was formed. A 10 mm test-tube, attached to the cold finger collecting the Xe batch via a 2 m length of nylon tubing, was dipped into the acetone slush bath. The valve connecting the pump to the test-tube and the Xe cold finger was opened briefly to evacuate the system and then closed. The cold finger was quickly submerged in warm water, causing the solid Xe to sublime, rapidly raising the pressure in the line to approximately atmospheric pressure. The pressure then dropped as the Xe condensed as a liquid in the test-tube. Once the pressure in the transfer line had stabilized, it was assumed that the system had reached equilibrium. It was found that 30-40 minutes of collection time yielded about 0.5 cm³ of condensed liquid Xe. The longitudinal relaxation time of liquid Xe is faster than in the solid so, following the condensation step, the experiment was immediately run.

3.5.2 Relaxation Experiments

A CPMG experiment was run on liquid Xe. Xe was condensed in a tube in the sweet spot of the ex-situ magnet following the previously described technique. Typical Xe volumes were in the region of 0.5 cm³. The liquid Xe T_2^* relaxation time in this region was measured to be in the region of 50 μ s. The echo time was kept the same as the echo time in the gas-phase experiment — 1 ms. Limitations on the amount of memory available meant that we could only collect 16000 echoes. We initially assumed that this would be more than sufficient. Figure 3.3(a) shows the integrated intensity of each echo *vs* time. Remarkably, over the period of 16 secs, the transverse magnetization had decayed only partially. The curve clearly shows a bi-exponential decay, with a rapidly decaying component for the first couple of seconds. This initial rapid decay could be due to geometric factors leading to an anisotropic dipolar field, or perhaps something as simple as enhanced wall relaxation until the pyrex surface had become saturated. Fitting the slow decay to a single exponential we obtained a T_2 of 36.1 s; one of the longest liquid state T_2 decay times on record.

There have been 3 other studies of the T_2 of liquid Xe. The record is held by Romalis and Ledbetter who observed a T_2 of 1300 s in hyperpolarized liquid Xe at

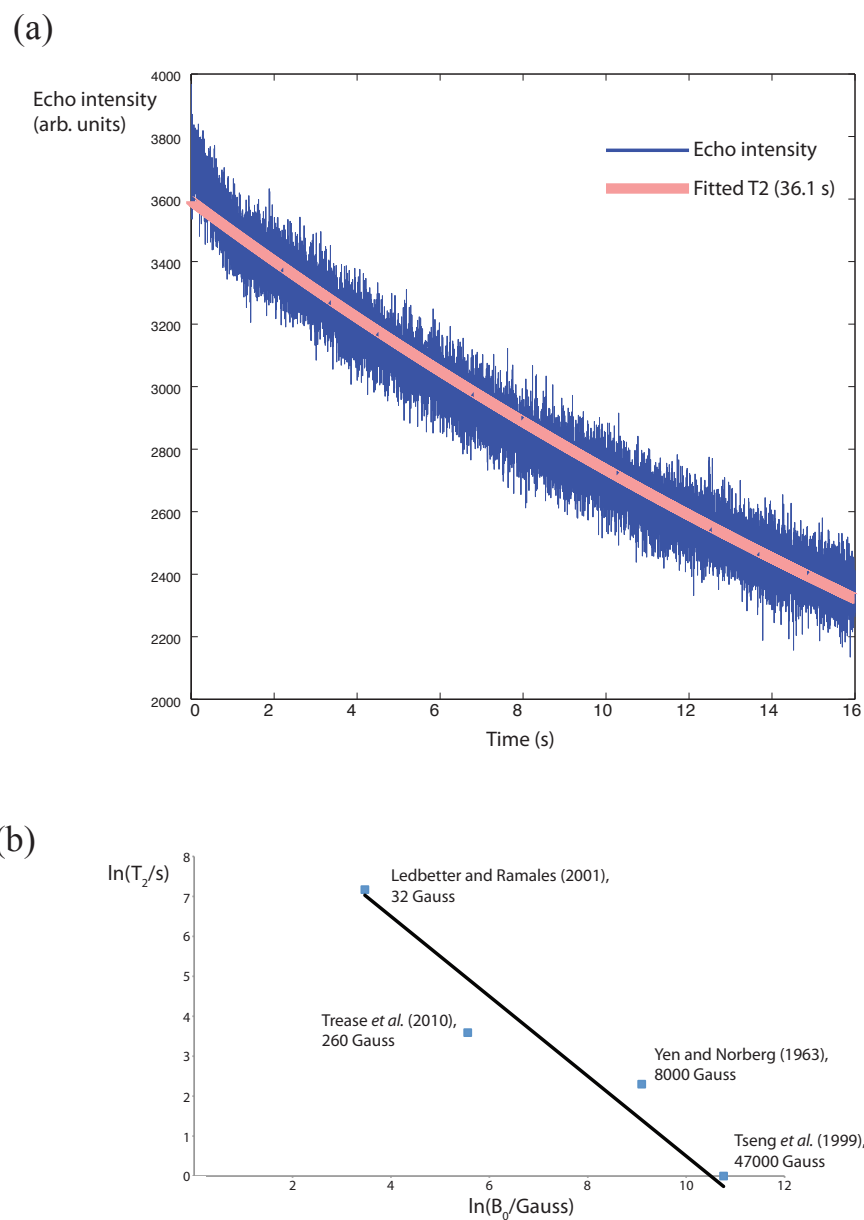


Figure 3.3: (a) Experimental T_2 decay curve (b) Collation of all liquid Xe T_2 data of which the author is aware

low field (32 Gauss) [52]. Yen and Norberg obtained a value of 10 s in thermal liquid Xe at 8920 Gauss [72]. Tseng et al. estimated 1 s in hyperpolarized Xe at 47000 Gauss [62]. All of these data were collected using a CPMG train of pulses. There appears to be a strong relationship between field strength and T_2 . The data are plotted in Figure 3.3(b) and a linear trendline added. The equation of the line is $T_2 = \frac{36000}{B_0}$. With so few points it is risky to draw any strong conclusions, however, other than the fact that there is a strong dependence of some sort. The study is complicated by the presence of strong dipolar fields in liquid hyperpolarized Xe. In these conditions there are very significant non-linear effects relating to the tip angle. Ledbetter observed that long T_2 values followed a 1 degree flip angle whereas, following a 90 degree flip, the T_2 was in the realm of one or two seconds. In our experiment we were using as close a pulse to a 90 as possible and were thus probably observing a T_2 of somewhat less than the maximum possible at 200 Gauss.

3.6 High Field Gas Phase Xenon T_2 Experiments

In order to use hyperpolarized gas to diagnose pulmonary function, a number of tools are available to the MRI scientist [2]. Measurement of spin density, longitudinal relaxation (T_1), transverse relaxation (T_2) and effective transverse relaxation (T_2^*) provide useful information in diagnosing and evaluating pulmonary function.

As we have seen, the T_2 for Xe in the liquid state is long. This is true for Xe gas as well. In homogeneous fields, the predominant transverse relaxation pathway is the interaction of Xe atoms with the container walls. Paramagnetic impurities in the walls lead to rapid T_2 relaxation. Dangling O and OH from the glass surface are also a significant source of small-scale inhomogeneity in the magnetic field. In order to prevent the Xe from interacting with the glass walls directly, containers are often coated in an inert material such as paraffin wax or siliconized, slowing down relaxation significantly.

Although Xe T_2^* has been investigated in the case of a model system, treating the lung as a porous medium [46], there have been no studies of lung disease based on the surface properties of the alveoli. Xe(g) should be a very sensitive probe for surface properties, the long T_2 leading to high contrast for small changes in the alveoli surface. However, the T_2 of Xe will also be a function of the geometry of the container. The ratio of surface area to volume increases with decreasing container size, increasing the number of wall collisions per unit time. The following experiments detail the as yet unpublished research [71] into the sensitivity of Xe T_2 as a function of container material and size, and its possible application in medical MRI.

We chose to compare the relaxation properties of Xe as a function of wall material

and vessel size. At high field the NMR spectrum of thermal Xe is sufficiently intense to record a T_2 relaxation curve, so hyperpolarization was not used. Twelve cylindrical thick-walled tubes were filled with pure natural-abundance xenon gas (26.4 % ^{129}Xe). Six tubes were made of Pyrex, and another six tubes were made of quartz. Of these, half were coated using Surfasil and the other half left uncoated. Thus there were four sets of 3 tubes, each set consisting of a different material and coating. The three different tubes were of different inner diameters (1.7 mm, 4.14 mm and 8.16 mm), in order to observe any geometric effect on the value of T_2 .

To reduce signal averaging time, high pressure Xe gas was used. The tubes were first charged with Xe up to the required pressure. They were then immersed in liquid N_2 , condensing the Xe as a solid. The tubes were flame sealed, and allowed to warm up in a padded reinforced container. The flame-sealing step is dangerous and was done professionally by the chemistry department glass blower, Jim Breen, using full protective equipment. The pressure in the tubes was recorded before condensation of the Xe gas and was typically around 65 psi. This method may not entirely accurately reflect the pressure after flame sealing, as the volume of the vessel will have changed slightly.

The experiments were run on a Varian AS400 400 MHz microimaging instrument (known in the lab as “the David Beckham”) with VNMRJ 2.2C software. In this field the Xe Larmor frequency was 110.57 MHz. In order to measure the T_2 of the phantoms we used a Carr-Purcell-Meiboom-Gill (CPMG) for all measurements. The very long T_1 of Xe (tens of minutes) necessitated the use of a very long relaxation delay between measurements; about 40 minutes.

In a well-shimmed commercial high-field NMR magnet, the field gradient in the probe volume is very small. Thus, in modeling T_2 we can ignore the effects of diffusion attenuation. We can broadly categorize the two significant contributors to T_2 in Xe gas as bulk and surface mechanisms. Bulk relaxation is due to collisions between Xe atoms. Assuming ideal gas conditions, the collision rate is proportional to the first power of the gas pressure. The surface relaxation, on the other hand, is a function of the rate of diffusion, which is inversely proportional to the pressure. As relaxation rates from different processes are additive, the total T_2 is given by

$$\frac{1}{T_2} = \frac{1}{T_{2,bulk}} + \frac{1}{T_{2,surface}} = Ap + \frac{B}{ap} \quad (3.2)$$

where p is the pressure, a is the radius of the tube and A and B are coefficients which depend on the bulk and surface properties, respectively. By measuring T_2 as a function of either pressure or radius of vessel we can determine A and B .

It can be seen from this equation that the surface relaxation rate is both a function of the vessel size and the surface material. Using this parameter, vessels such as

alveoli that have both different surface properties and sizes will be indistinguishable. Thus $T_{2,surface}$ is not a particularly reliable parameter to characterize intrinsic surface properties when we have no *a priori* knowledge of vessel size. It would be more powerful for the spectroscopist if we could separate this parameter into independent geometric and material parameters. Fortunately, the theoretical background for this was presented in 1978 by Brownstein and Tarr [7]. The surface relaxation rate can be written as

$$\frac{1}{T_{2,surface}} = \frac{D\eta_n^2}{a} \quad (3.3)$$

where D is the diffusion rate of the gas and η_n are the positive roots of

$$\eta_n \frac{J_1(\eta_n)}{J_0(\eta_n)} = \frac{Ma}{D} \quad (3.4)$$

in terms of the cylindrical Bessel functions.

Utilizing these equations, the true surface relaxivity, M , can be calculated. The results obtained, correcting for pressure, are plotted in Figure 3.4 and tabulated in the table below

Surface relaxivities				
I.D. (mm)	Uncoated Pyrex	Coated Pyrex	Uncoated Quartz	Coated Quartz
1.7	2.47×10^{-2}	5.4×10^{-3}	3.4×10^{-3}	4.0×10^{-4}
4.14	2.49×10^{-2}	5.7×10^{-3}	3.9×10^{-3}	4.3×10^{-4}
8.16	2.54×10^{-2}	5.3×10^{-3}	3.6×10^{-3}	4.2×10^{-4}
Mean	2.5×10^{-2}	5.5×10^{-3}	3.6×10^{-3}	4.2×10^{-4}
Error	$\pm 1.5\%$	$\pm 3.6\%$	$\pm 6.2\%$	$\pm 3.5\%$

It is clear from these data that $\frac{1}{T_{2,surface}}$ is both a function of the size and shape of the tubes, as predicted (Figure 3.5). It is also clear that the surface relaxivity, M , is independent of vessel size but dependent on the surface material. For both materials, coating the material with Surfasil made an order of magnitude improvement in T_2 relaxation time. Relaxation on the surface of pyrex was considerably faster than that of quartz both before and after coating. This is probably due to a higher concentration of iron-based impurities in the pyrex. The fact that the quartz tube showed much better relaxation properties even after coating was a surprise. It is often assumed that once the material is coated, the relaxation properties become predominantly a function of the coating material. Here this is clearly not the case. This could have

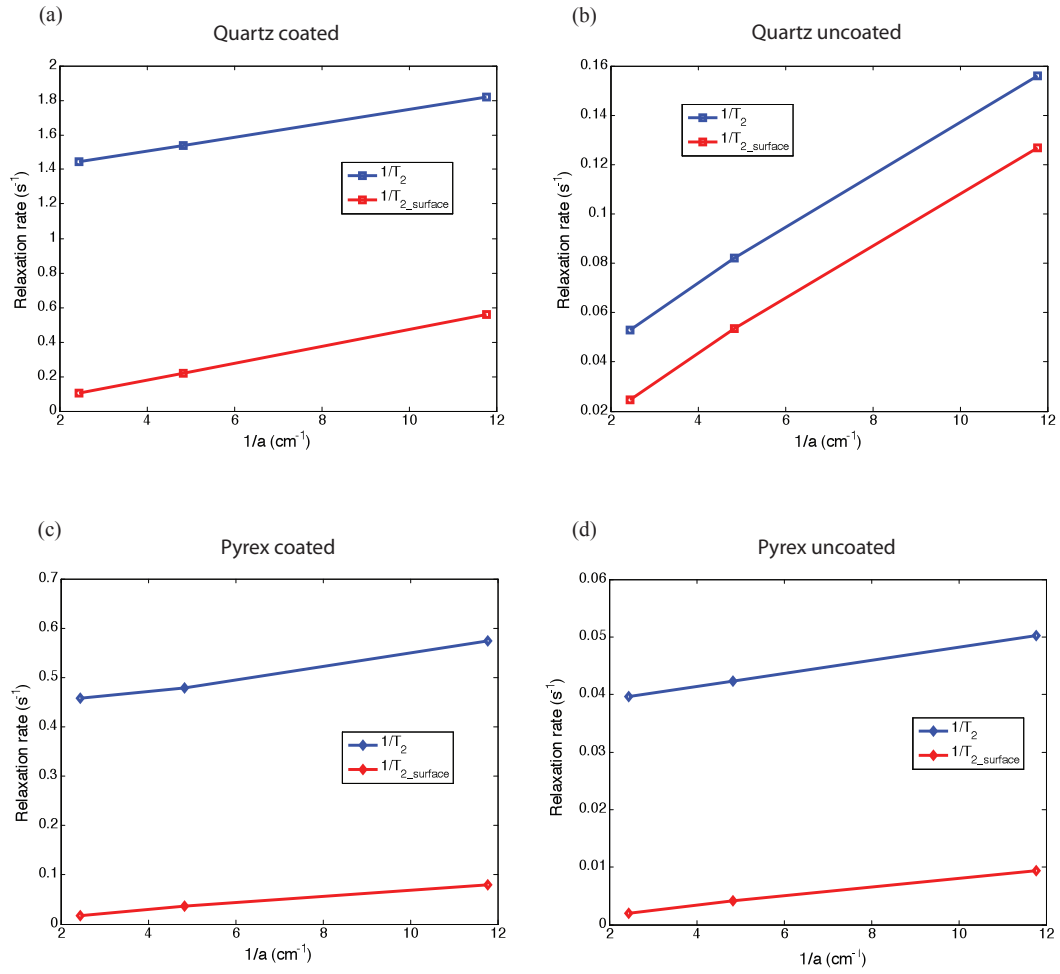


Figure 3.4: The transverse and surface relaxation rates as a function of $1/a$

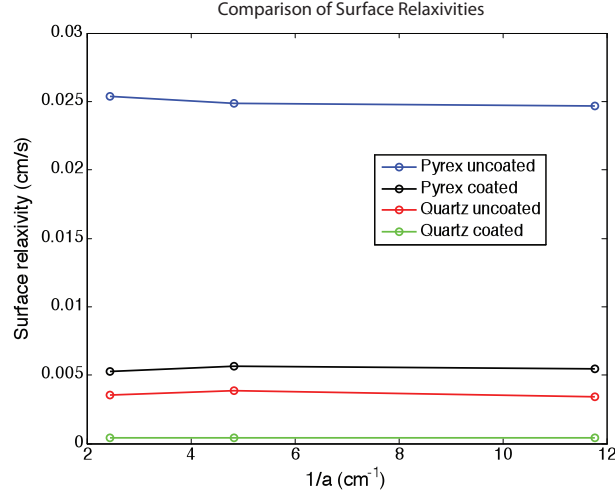


Figure 3.5: Surface relaxivity, M as a function of $1/a$

implications for the study of the surface properties of alkali vapor cells [3], where there is a strong emphasis on coating type but very little on the nature of the glass itself.

Across the data the errors were small, indicating that this could be a robust technique for determining the nature of a surface in more experimentally challenging conditions than a glass cell. For example, many lung diseases, such as pulmonary fibrosis, are associated with physiological changes in the surfaces of alveoli. To probe the surface relaxivity, it would be necessary to measure the diffusion coefficient in the lung, the lung structure and obtain an image of $T_{2,surface}$ across the lung cavity. With these data, a map of surface relaxivity, M , could be derived. Assuming that the volume of the affected region of the lung is comparable to the voxel size, the diseased regions of the lungs would show up as variations in the value of M . This technique offers advantages over current techniques. It is independent of the size of the alveoli, where more conventional T_2 maps are dependent upon it. It could therefore be expected to be more sensitive to pathologies for which the surface is changed but the size of the alveoli unaffected. Furthermore, this method could easily be modified for the study of other materials where bulk surface information is hard to obtain using other means.

Chapter 4

Diamond NV Magnetometry

In our macroscopic world we like things to be consistent. We like to throw an orange and find that it flies away from us. We don't like it when, on third throw, it flies away at 90 degrees and then teleports through a wall. Fortunately we don't generally have to worry about such inconsistencies. It's only the poor quantum physicist who has to worry about his particles behaving irrationally. In fact, the quantum physicist would love to be in control of his nanoscopic orange at all times. Or failing that, have a good idea of when and if it will do unexpected things. This, in a nutshell, is the field of *quantum control*.

The issue of control of quantum systems is not just an idle curiosity. It lies at the very heart of what is being hailed by some as the “second quantum revolution” [18]. Where the first quantum revolution in the early 20th century gave us the laws governing the microscopic realm, the second quantum revolution, so it is said, will exploit these rules to develop fantastic new technologies. At the forefront of this revolution are the fields of nanotechnology [40] and quantum information processing (QIP) [48]. The fields are very much interdependent; it is likely that the development of the first useful quantum computer will be more due to advances in nanofabrication than in quantum information theory. The riches promised by the second quantum revolution are great indeed; uncrackable encryption, super-fast computers and even nanomachines sailing around in your bloodstream. Of course, between here and this future technological wonderland there are a number of quantum hurdles. Chief amongst these hurdles, particularly for QIP, is that of decoherence.

The simple Hamiltonians used to accurately describe the evolution of quantum systems are ultimately just approximations to the Hamiltonian which truly describes the system. In liquid-state NMR, for example, we make the sweeping assumption that every chemically indistinguishable molecule is identical. However, we know this not to be the case — each particle has its own unique spatial location. In homogeneous

fields over short timescales this approximation is valid and we can usually view our system as evolving purely under the effects of chemical shift and J-coupling. However, as described in chapter one, small differences in local magnetic field lead to differential phase acquisition for each spin. We usually model this as the T_2^* decoherence. It would perhaps be more enlightening to treat the evolution of each spin individually, accounting for the variation in field strength across the ensemble. Though horrendously complex (the Hamiltonian in matrix form would have trillions of individual terms), we would gain a fuller picture of the evolution of the system and no longer need to invoke the rather mysterious force of T_2^* decoherence. Unfortunately even this Hamiltonian would not suffice as it does not take into account dipolar coupling between molecules, molecular collisions, wall relaxation, etc, etc. So after generating our huge Hamiltonian we would still see decoherence, albeit on a slower timescale (in this case, T_2). Sweeping aside the complications of determining the initial wavefunction of the ensemble, there is no conceivable way of determining the true Hamiltonian (to do so would require knowledge of the quantum state of the universe [29]). But, just imagining that we could, then we would not need to invoke relaxation at all. In fact it could be argued that decoherence is actually a form of coherent evolution — just evolution under a mind-bogglingly complex Hamiltonian.

The end product of decoherence is essentially a loss of information. For most experiments this is very bad indeed (though, as mentioned in Chapter 1, the rate of decoherence can actually provide useful information in some cases). For spectroscopic measurements, linewidth, and thus resolution, is directly related to the lifetime of a state. In quantum computation the decoherence lifetime limits the duration of a quantum gate [17]. Unfortunately there is a strong relationship between the addressability of a quantum system and its coherence lifetime; in general it is found that many promising QIP candidate systems are strongly coupled to their surroundings and rapidly decohere.

The search for systems which break this trend has uncovered a number of interesting candidates. One of the most promising is the diamond nitrogen-vacancy (NV) defect center. Its easily addressable spin state and long electron coherence lifetime make it a frontrunner in the hunt for a useful scalable quantum computer. However, applications of this fascinating system do not stop there; very high photostability makes it an attractive candidate for use as a fluorescent marker, while work has begun on its implementation as a sensitive high-spatial resolution magnetometer. The remainder of this dissertation will concentrate upon the latter usage and detail our work to date in building an NV magnetic resonance detector.

One of the major research thrusts of this lab is the development of low-field magnetometers for applications in zero-field NMR [38], low field MRI [70] and, recently, low-field J coupling spectroscopy. These experiments have all been run on Rb vapor-cell magnetometers. Alkali vapor magnetometers detect the change in the rotation

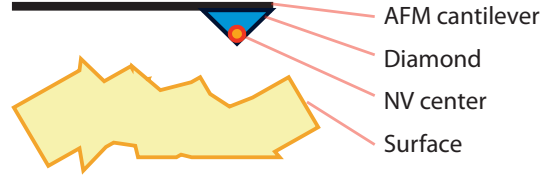


Figure 4.1: Cartoon of cantilever-based NV surface magnetometry

of plane-polarized laser light through an optically pumped alkali metal vapor, caused by the presence of a magnetic field. They have been very successful in measuring extremely low magnetic fields, with a comparable field sensitivity to superconducting quantum interference devices (SQUIDs); DC: $160 \text{ aT}/\sqrt{\text{Hz}}$ [14], AC: $240 \text{ aT}/\sqrt{\text{Hz}}$ [39]; but with a fraction of the running cost. However, the spatial resolution in an MRI experiment run using one of these devices is fairly poor. Ultimately there is still the constraint imposed by size of the gradient applied in during the encoding stage of the MRI experiment. In principle, this limitation could be overcome by making the magnetometer very small and scanning it over the substrate of interest, obviating the need for a conventional gradient. Whilst work continues on the miniaturization of the vapor cell [35], there is a fundamental size limit imposed by the necessity to heat the cell and by the thickness of the cell walls. Thus, a vapor cell of dimensions smaller than a few hundred microns is unlikely to be realized.

The highest resolution yet realized in a nuclear magnetic resonance imaging experiment, about 10 nm per voxel, was actually achieved using magnetic resonance force microscopy (MRFM) [15]. This impressive result comes with the caveat that the image required days to acquire and the substrate, in this case the tobacco mosaic virus, needed to be cooled to cryogenic temperatures.

The most recent contender in the field of ultra high-resolution MRI is the diamond NV magnetometer. Recently an MR image of a magnetic structure with a resolution of 20 nm was demonstrated, using a single NV attached to the tip of a cantilever [4](Figure 4.1). The magnetic field sensitivity in this experiment was very low, about 0.5 mT, but as the technique advances, orders of magnitude improvement can be expected.

There is significant promise not only in single NV centers for ultra-high resolution MRI but in bulk diamonds for use as cheap, high sensitivity magnetometers. In this case "bulk" need not mean "large". Diamonds a few tens of microns in diameter are perfectly adequate. The technology required for the operation of a bulk magnetometer is very cheap and scalable. At its simplest, all that is required is a diamond, a green LED, a photodiode, and a microwave transmitter. The price and size of the latter

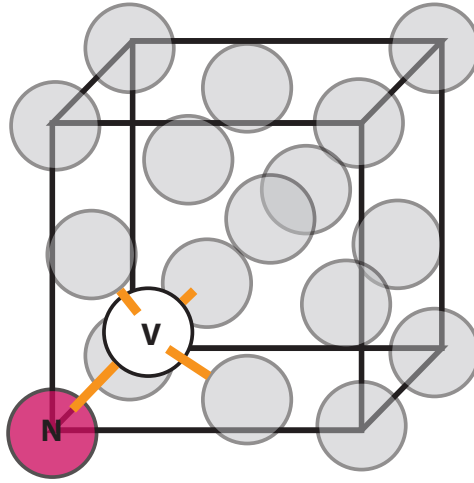


Figure 4.2: Crystal structure of NV center

has dropped hugely over the last 20 years with the advance of cellphone technology, and particularly with the recent work in WIMAX technology.

We have constructed a diamond NV magnetometer for use in NMR experiments in the lab. We have run magnetometry experiments, initially obtaining a field sensitivity of about one hundred nanotesla. This research is an ongoing priority for the lab. The experimental results so far obtained are detailed in the remainder of this chapter.

4.1 Properties of the Diamond NV Center

4.1.1 Structure

The NV center is just one of over 100 types of identified defect in the diamond lattice. Often the presence of a high concentration of a particular defect leads to coloring in the diamond; in the case of nitrogen, the associated color is pink, or purple at very high N concentration.

There are two ways of generating synthetic diamonds commercially. High pressure, high temperature (HPHT) synthesis works by heating and compressing graphite until it undergoes a phase transition to diamond. Chemical vapor deposition (CVD) works by growing a diamond from a seed diamond and a hydrocarbon gas mixture. Generally the ambient concentration of N atoms in the crystal is sufficient for use in NV spectroscopy but if high concentrations are required techniques such as fast ion implantation can be used to add more. The diamond then undergoes irradiation,

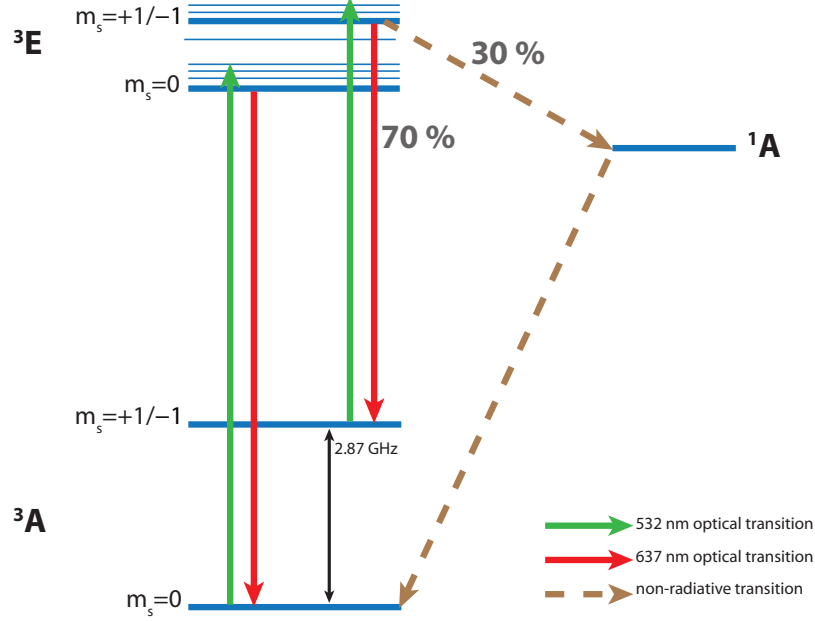


Figure 4.3: Energy levels in the NV center

generally using electrons or protons, to increase the vacancy concentration. Finally it is annealed at around 700 C to allow the N atoms and vacancies in the lattice to diffuse together, to form an NV center.

The NV is composed of N^- coupled with a C vacancy. The lone pair of the N is located in the vacancy in the crystal lattice. The vacancy possesses C_{3V} symmetry. This point group has 3 possible irreducible representations, A_1 , A_2 and E. Low temperature studies have shown that the ground state is 3A_2 , with the 3A_1 and 3E excited states closely spaced together. At high temperature, for reasons not yet clear, the 3A_1 and 3E become degenerate, and are generally referred just as 3E . In the ground and excited states, coupling of the spin triplet with the diamond crystal field splits the three possible triplet spin states: $m_s = +1, 0$ and -1 into two sublevels, $m_s = 0$ level and a degenerate $m_s = +1/-1$ level [33].

The ground state energy difference between the two sublevels in the absence of a magnetic field (known as the zero-field splitting) is 2.88 GHz. Interestingly, in the excited state, the zero field splitting is almost exactly half the size, 1.42 GHz. Whether this is significant or a coincidence is not yet known [42]

4.1.2 Coherence Lifetime

One particular characteristic of the NV center is its unusually long electron T_2 coherence time. The long coherence lifetime of the NV center results from the weak electron-lattice coupling. Strong dipole-dipole coupling between the electron and a neighboring spin usually leads to fast decoherence in solids. However, in diamond there is no such relaxation pathway. The neighboring atoms are mostly ^{12}C which is nuclear spin 0. In low-N diamonds the main decoherence pathway is through coupling with the small quantity of natural abundance spin $1/2$ ^{13}C in the lattice. In high-N concentration diamonds the primary decoherence source is coupling with paramagnetic neutral N in the lattice. Recent experiments using ^{12}C enriched, low N diamond have shown NV electron coherence times of milliseconds — an eon in terms of solid-state electron lifetimes [5].

Coherence lifetime is crucially important for magnetometry applications. In general the fundamental sensitivity of a magnetometer is inversely proportional to the square root of the coherence lifetime of the detector [52]. The presence of a magnetic field can be detected by observing the phase acquired during electron free precession. The accrued phase increases with time, so a longer coherence lifetime allows for the build-up of a greater amount of phase and thus the detection of smaller magnetic fields.

4.1.3 Optically Detected Magnetic Resonance

For most systems the spin state is inferred from the measurement of ensemble magnetization; either inductively, in a coil, or using a magnetometer such as a Rb-vapor cell. It would, in theory, be possible to detect the spin state of the electrons in diamond in a similar way, by directly detecting the precessing electron magnetization. However, the signal from the electrons would be minute and of a very short lifetime. Fortunately, the NV center provides a mechanism for a much more sensitive spin readout — optical detection. Optically detected magnetic resonance, (ODMR) offers the spectroscopist the sensitivity advantages inherent to optical systems. ODMR methods include direct observation of Faraday rotation of polarized light and optical rotation of light using alkali metal vapor cells.

The ODMR technique in NV spectroscopy is slightly unusual, taking advantage of a quirk in the electron relaxation pathway (Figure 4.3). Optical excitation from the ground state (^3A) to the first electronic energy level (^3E) is spin conserving, so $m_s=0 \rightarrow m_s=0$ only, $m_s=+1 \rightarrow m_s=+1$ only and so on. From the excited ^3E state, relaxation is fast, the excited state lifetime being of the order of nanoseconds. Most of the relaxation is in the form of fluorescence back down to the ground state. However, electrons in the $+1$ and -1 states have a different relaxation pathway available; non-

radiative decay to the metastable 1A state, followed by non-radiative return to the ground state. This pathway accounts for up to 30 % of excited state $m_s=+1/-1$ electrons. Thus, when there is a significant population in the $m_s=+1/-1$ state there is a drop in fluorescence intensity. In this way we can optically determine the population difference between the $m_s=0$ and $m_s=+1/-1$ states

At room temperature, the energy difference between the two ground state sublevels is small; 2.88 GHz. This leads to a very small thermal population difference. The NV system provides a mechanism for hyperpolarization of the $m_s=0$ level, closely related to the mechanism for ODMR.

The final relaxation step of the non radiative pathway, following optical excitation of an $m_s=+1/-1$ electron, is decay from the metastable 1A state to the ground state. This step selectively populates the $m_s=0$ sublevel of the ground state only. So, it can be seen that just by application of laser light, the $m_s=+1/-1$ sublevel is depopulated and the $m_s=0$ level filled. Optical pumping in NV centers is very efficient, reaching close to 100 % polarization of the $m_s=0$ sublevel.

4.2 Experiments

4.2.1 Continuous Wave NV Magnetometry With DC Magnetic Field

In the presence of an applied magnetic field the degeneracy of the $m_s=+1/-1$ sublevel is lifted by the Zeeman interaction. Thus, the difference between the $m_s=+1$ and $m_s=-1$ energy levels is a reporter for the size of the magnetic field at the NV center, the energy gap given by $2\gamma_{(\text{electron})}$. In principle the size of the Zeeman interaction could be probed by direct absorption spectroscopy. The microwave frequency could be swept, and the resonant excitations observed by the absorption of the microwave energy. However, probing the populations optically, in the ODMR mode, is considerably easier and more sensitive.

In its simplest incarnation, a diamond magnetometer is very easy to construct (Figure 4.4). The first generation magnetometer in the lab took no more than a couple of days to put together, once the components were available. Optical excitation of the diamond was provided by a 1.3 W green 532 nm diode-pumped (DPSS) laser (OEM Laser Systems). The laser light simultaneously provided the optical pumping and the ODMR probe photons. Initially laser powers of a couple of hundred mW were used, but it seems that signal to noise is unaffected by dropping this down to a few tens of mW or below.

A diamond with N concentration of about 1 ppm [1] was attached to a glass slide

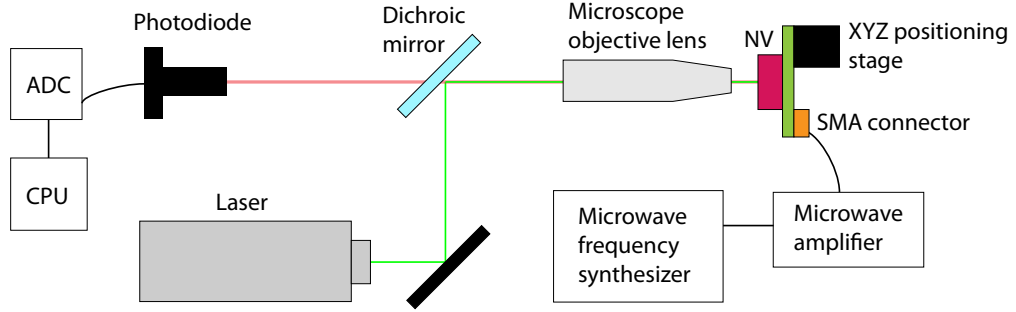


Figure 4.4: Block diagram of a simple diamond NV magnetometry experiment

with cyanoacrylate glue (Figure 4.5). The glass slide was mounted onto a circuitboard consisting of a microwave stripline terminated at both ends with an SubMiniature version A (SMA) male connector. A microscope objective lens (extra-long working distance, aperture 0.4, working distance 11 mm, $20\times$ magnification) was used to focus the laser light onto a small spot on the diamond. Red fluorescence photons were collected using a photodiode (Thorlabs PDA 100A) placed close to the diamond and equipped with a low-pass filter to screen out the scattered green light. A dichroic mirror was used to further filter the green light from the fluorescence signal. The photodiode output was connected to the input of a DAC (National Instruments USB-6215). A microwave waveform, generated by a PTS 3200 RF frequency synthesizer, was amplified using a high-frequency solid-state amplifier (Mini Circuits ZHL-16W-43-S+) and connected to one of the SMA connectors on the stripline. The other end of the stripline was terminated using a 50 ohm terminal. Under continuous-wave laser excitation, the microwave frequency was swept across the desired spectrum and the drop in fluorescence due to on-resonant microwave excitation of the $m_s=+1$ and $m_s=-1$ sublevels was recorded.

Barring the high-NV concentration diamonds, for which there is currently no commercial source, the only expensive item in this setup is the microwave frequency source. A stable 3 GHz microwave variable frequency generator such as a PTS costs in the region of \$15,000. This can be circumvented by applying a large leading field of around 1000 Gauss to the diamond, reducing size the $m_s=0 \rightarrow m_s=+1$ transition to a few MHz. At this frequency, the price of RF electronics drops considerably. It is also possible to bypass the variable frequency generator altogether by using a monolithic single-frequency microwave synthesizer and mixing the output of this with a varying RF baseband from a simple function generator.

In our first experiment on the newly constructed magnetometer we wanted to observe the effect of changing the position and orientation of a magnet with respect

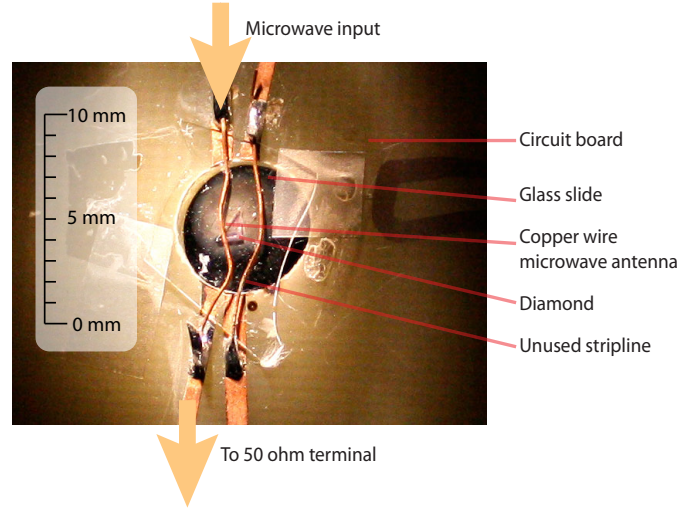


Figure 4.5: Diamond mount

to the diamond. This was mainly an exercise in getting used to the experimental apparatus but yielded some interesting results.

The applied microwave excitation was swept across a broad range of frequencies in steps of 5 MHz. The large step size was necessary as the frequencies were being changed by hand at the PTS console; a laborious process. We observed the drop in fluorescence upon excitation of the $m_s=0 \rightarrow m_s=+1$ and $m_s=0 \rightarrow m_s=-1$ transitions by connecting the photodiode to an oscilloscope and recording the voltage drop by hand. The microwave was run at full power: 44 dBm (25 W), a value probably far higher than was required. At this power level there was significant heating in SMA cables and the 50 ohm terminal placed after the microwave stripline.

A small (~ 1 cm diameter) rare earth magnet was moved closer to the diamond between the acquisitions of each spectrum, changing the field strength and field orientation at the diamond (Figure 4.6). Initially, in Earth's field we see a single resonance, corresponding to the transition between the $m_s=0$ and the apparently degenerate $m_s=+1/-1$ sublevel. In the Earth's field of approximately 0.5 Gauss the splitting of this sublevel should be about 2.8 MHz. The fine structure due to the Zeeman interaction with the Earth's magnetic field is obscured by the broadness of the peak — about 20 MHz at half max.

Upon increasing the applied field strength, by bringing the magnet closer to the crystal we see the Zeeman interaction initially splitting this peak into two, and then into multiple resonances. The presence of multiple lines in high magnetic fields is expected. There are four different possible orientations of the NV center, arranged

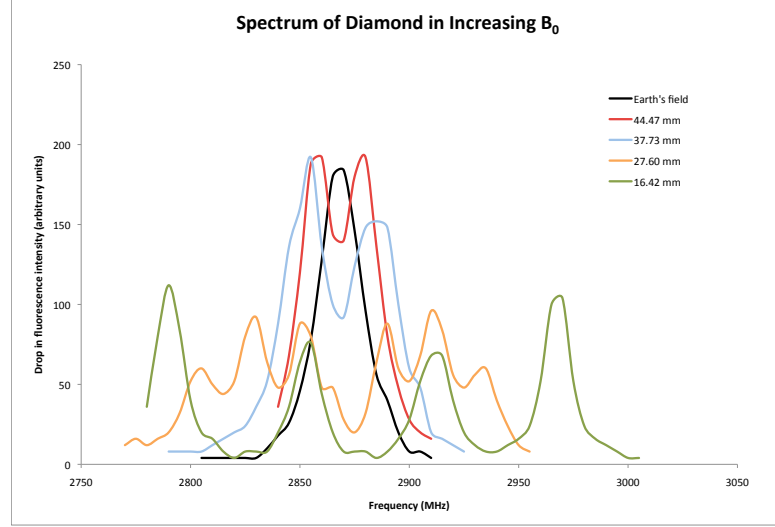


Figure 4.6: Spectrum of the NV center in varying field strengths, controlled by changing the distance from a rare-earth magnet

tetrahedrally. The projection of the magnetic field along the principle axis of each of the four different orientations will, in general, be different. Thus, making the valid assumption that there is an equivalent amount of NV centers of each orientation in the sample, there are actually four different Zeeman transitions present. Once the applied field is high enough, the difference in Zeeman splittings becomes greater than the linewidth and the multiplet structure becomes apparent.

Because of the broadening caused by the presence of multiple orientations, it is preferable to selectively observe just one transition. The easiest way to do this is to apply a large enough leading field in order to split the four orientations apart and then just observe one of these peaks.

By changing to remote control of the frequency we were able to obtain higher-resolution spectra of the NV system (Figure 4.7). It is clear that even in Earth's field there is a splitting of the $m_s = +1/-1$ sublevel. This splitting is in the region of 6 MHz — somewhat larger than would be expected from the Earth's field alone (about 3 MHz). It is due, in fact, to the stress in the crystal. In generating the diamonds, generally through chemical vapor deposition (CVD), minute stresses are grown into the structure. This leads to distortion of the crystal, such that the local axial C_{3V} symmetry is broken. The splitting is parameterized by the parameter, E , and is visible

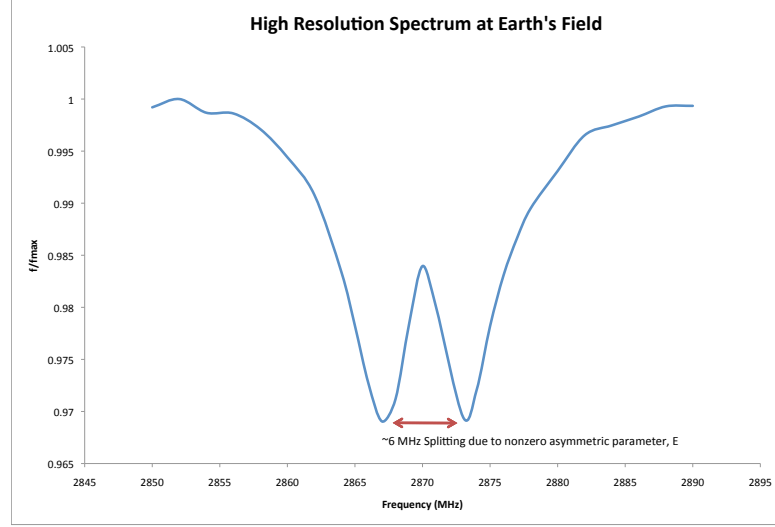


Figure 4.7: Earth's field ODMR spectrum of the NV center

in all the high-resolution spectra that were taken. The distribution of stress across the crystal is highly anisotropic, with some regions retaining axial symmetry [25] and exhibiting no E-splitting whilst others show E values greater than 6 MHz. Thus, there is a distribution of different E values across the ensemble, manifesting itself as line broadening in the spectrum.

4.2.2 Continuous Wave NV Magnetometry With AC Magnetic Field

In order to overcome the effect of certain sources of noise, the experiment can be run in an AC mode. The amplitude of the fluorescence is modulated at a chosen frequency and only the Fourier component of the time domain signal at this particular frequency is measured. In this way, high frequency noise is ignored. In order to modulate the amplitude of the NV fluorescence, it is possible to modulate either the frequency of the applied microwave radiation or the amplitude of an applied magnetic field. In the former case, the microwave frequency is modulated around a center frequency and the center frequency gradually swept across the spectrum. In the latter case, an applied magnetic field oscillates at a given frequency, modulating the size of the Zeeman interaction, while the microwave frequency is swept, to generate

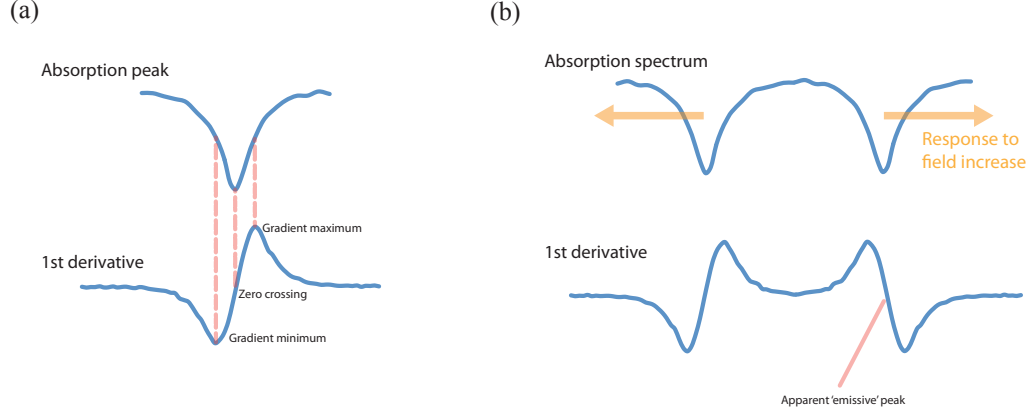


Figure 4.8: (a) Comparison of direct spectrum and first derivative (b) Phase difference in response of $m_s=+1$ and $m_s=-1$ leading to "emissive" 1st derivative peak

a spectrum.

Following the initial DC field experiments it was decided to move on to AC field measurements, in order to improve resolution. Due to technical limitations, we decided initially to use field modulation rather than microwave frequency modulation. The diamond was placed at the centre of a Helmholtz coil (radius=12 cm). The current modulating waveform was generated by a function generator and amplified using a gradient amplifier (Techron LVC2016). The strength of the field for a given applied current was calibrated using a 3-axis flux gate and measured to be about 2.4 G/A, or 1.25 G/V. The photodiode was connected to a lock-in amplifier (Stanford SR830 DSP). The lock in amplifier takes, as an input, the modulated fluorescence intensity as a function of time and outputs the amplitude of the chosen Fourier component. This value is equal to the gradient of the peaks on the direct spectrum. Thus, spectra generated using the lock-in amplifier are the 1st derivative of the direct spectra (Figure 4.8(a)).

The 1st derivative of the acquired spectra gives us a little more information than just the gradient. As the field strength is modulated, the absorption peaks move due to the change in the Zeeman splitting. The peaks corresponding to $m_s=+1$ move to lower frequencies with increasing field strength, while the peaks corresponding to $m_s=-1$ move to higher frequencies. The π phase difference in the response of $m_s=+1$ and $m_s=-1$ to the modulating field shows up as a relative inversion in the gradient of the peak, so that it looks "emissive" rather than absorptive. This phase difference enables us to unambiguously assign $m_s=+1$ and $m_s=-1$ energy levels, even for relatively complex multiplets (Figure 4.8(b))

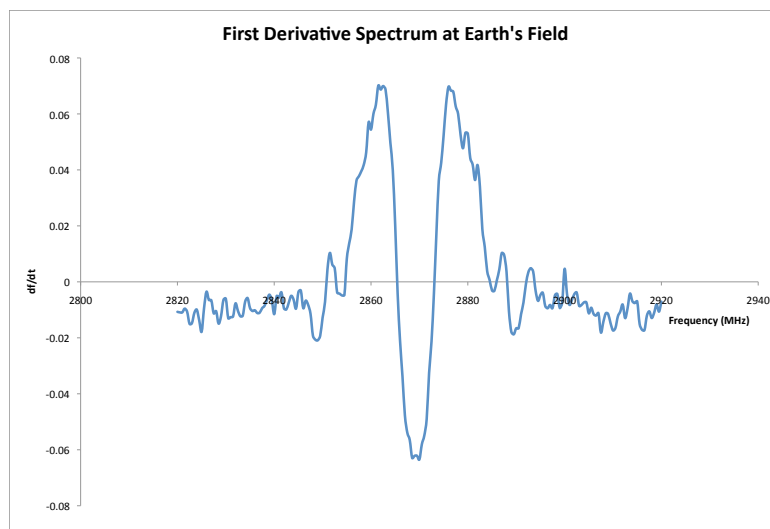


Figure 4.9: First derivative spectrum at Earth's field

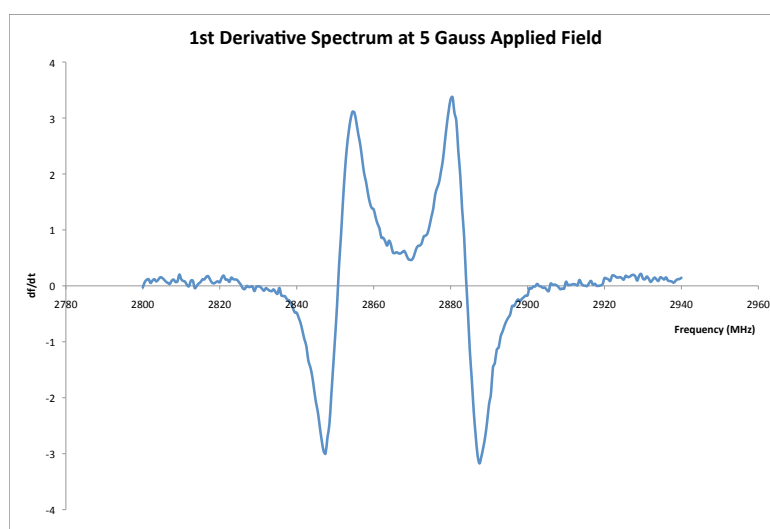


Figure 4.10: First derivative spectrum at 5 Gauss

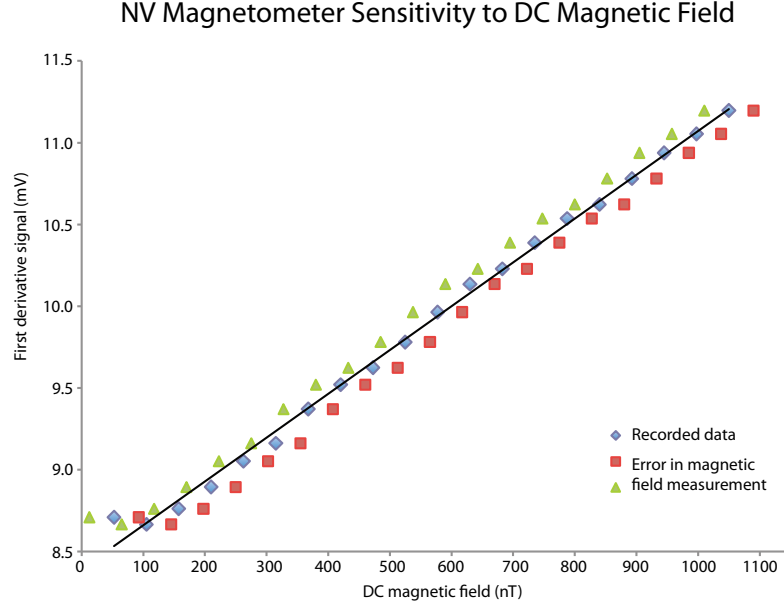


Figure 4.11: NV magnetometer sensitivity to DC magnetic field

An example spectrum at Earth's field is shown in Figure 4.9. A spectrum in 5 Gauss applied field is shown in figure Figure 4.10.

The eventual aim of this series of experiments is to observe nuclear magnetization. In order to establish whether this was yet possible, the sensitivity both to AC and DC magnetic fields was determined. A solenoid was used as a magnetic field phantom, to simulate the effective field from a hypothetical water channel. The solenoid consisted of about 20 turns of copper wire, forming a cylinder about 5 cm long, and was placed as close as possible to the diamond. The field generated by the solenoid was calibrated against the applied voltage by using a 3 axis flux gate. Uncertainty in the magnetic field measurement was in the region of ± 40 nT. This error is given in the x axes in Figures 4.11 and 4.12.

First, the DC sensitivity was calculated. Application of a small DC field will lead to a slight shift of the peaks in the spectrum. At some limiting value of applied field the shift will no longer be visible, falling below the noise threshold, in this case predominantly set by laser noise. It is still preferable in this case to use AC magnetic field modulation to improve sensitivity; the DC component being added onto the modulated field. The magnetometer will be most sensitive to a small DC field when the microwave excitation frequency is set at a maximum in the first derivative spectrum. A small shift in peak position will then show up as a sharp drop in the

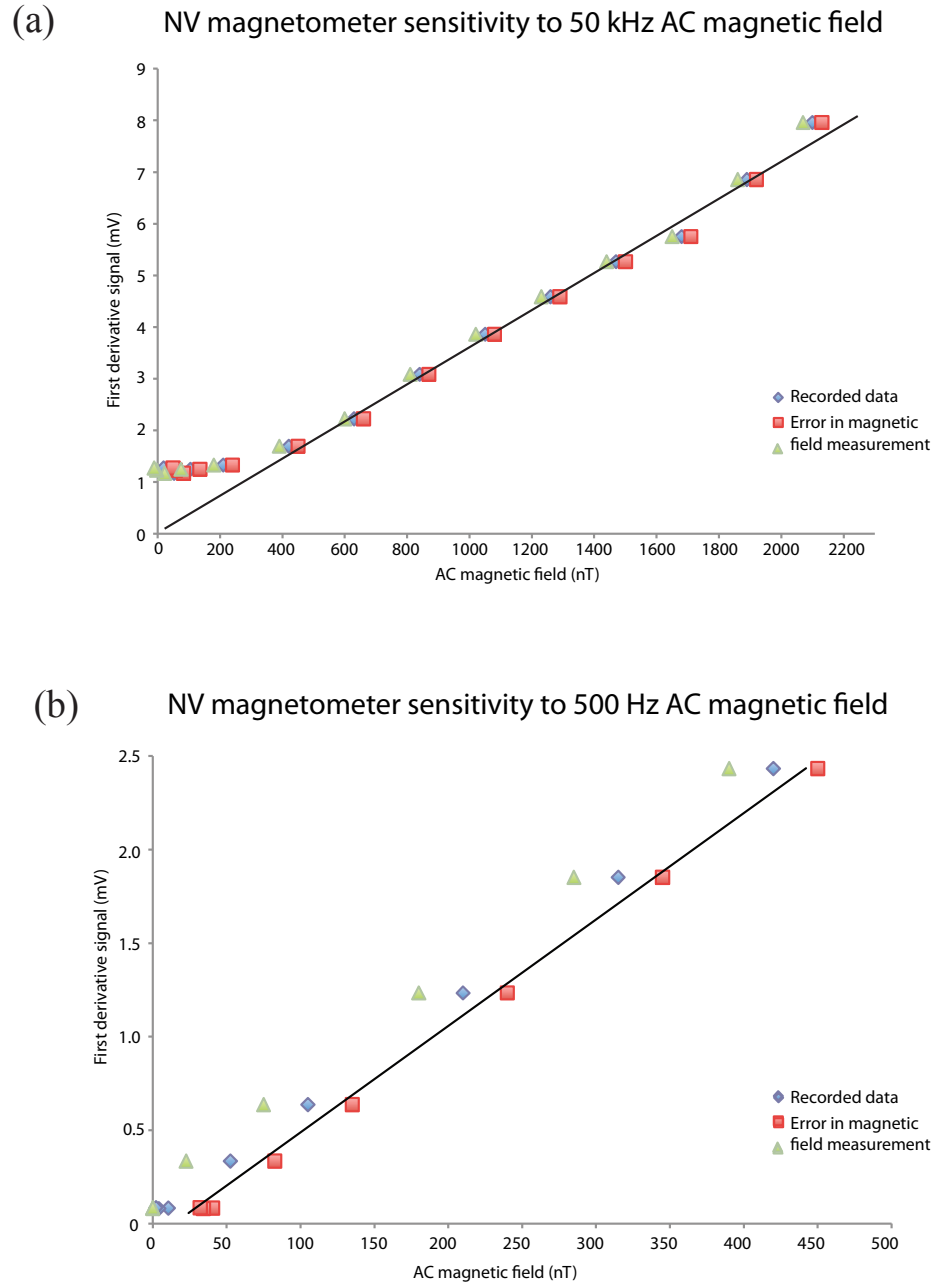


Figure 4.12: NV magnetometer sensitivity to AC magnetic fields

lock-in signal.

The magnetic field modulation was applied using a Helmholtz coil as before. The microwave frequency was set at a maximum in the first derivative spectrum. The DC voltage in the phantom was then increased and the drop in lock-in signal was recorded, signal averaging for about 100 s. The results are shown in Figure 4.11. Uncertainty in the accuracy of the magnetic field calibration makes statement of a definitive sensitivity difficult. The noise limit in the CW field measurement appears to be around 100 nT. Linearity begins at around 200 nT.

We then measured the sensitivity to a sinusoidal AC modulated magnetic field generated by the phantom solenoid. Again, the frequency of the applied microwave excitation was picked to give the maximum signal from the lock-in amplifier. Then the output from the lock-in was recorded for different applied AC voltages. The results are shown in Figure 4.12.

The sensitivity at high modulation frequencies, around 500 nT were surprisingly poor (Figure 4.12(a)). This is close to the bandwidth of the photodiode and the maximum frequency of the lock-in amplifier. High frequency laser noise at 50 kHz could also have interfered. The sensitivity at low frequency, 500 Hz, was considerably more encouraging (Figure 4.12(b)). After 100 s of averaging, fields of 50 nT were clearly visible. This is only an order of magnitude greater than the expected magnetic field generated by prepolarized water (see following section).

4.3 Dipolar Field Calculations

With the current sensitivity parameters sketched out, the next step is to plan the water NMR detection experiment.

4.3.1 MATLAB Coding

Knowledge of the strength and orientation of the magnetic field generated by an ensemble of nuclear spins is important for magnetometry applications. It is useful to have an order of magnitude estimate for whether an experiment is feasible before going to the trouble of building it. There are a number of commercially available programs that can be used to determine the magnetic field at an arbitrary distance from a magnetized surface, foremost amongst these being Femlab. This software uses finite element analysis to solve the field generated by a coarse grained mesh of points located on the surface on an object. This approach is not necessarily optimal for the purpose of calculating the magnetization of an ensemble of magnetic dipoles, where the surface remnant field is not known. For this purpose a MATLAB script was

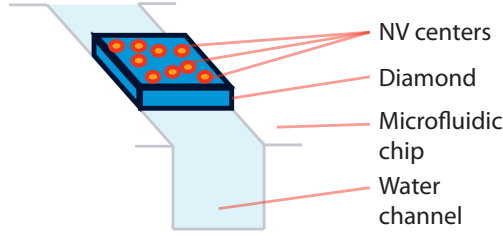


Figure 4.13: Cartoon of the envisioned position of the NV diamond relative to the water channel

written which takes as an input the chemical information about the ensemble, the magnetic properties of the nuclei, and the shape of the container and outputs the strength and orientation of the surrounding magnetic field.

Calculation of the field at a position far from a magnetized volume is easy. In this situation one can approximate the volume to a point dipole. The magnetic field, B is then given by

$$\vec{B}(x, y, z) = \frac{\mu_0}{4\pi} \frac{3\vec{r}(\vec{\mu} \cdot \vec{r}) - \vec{\mu}r^2}{r^5} \quad (4.1)$$

where μ_0 is the permeability of free space, $\vec{\mu}$ is the magnetic moment vector, \vec{r} is the position vector relative to the dipole and r is the absolute distance between the dipole and the measurement location.

This approximation breaks down for points in space that are closer than about 5 times the diameter of the magnetic volume. In this situation it is necessary to coarse grain the magnetic volume into smaller volumes, treating each of these as its own point dipole. The script entitled "dipolar field calculator" carries out this operation, coarse graining the lattice to arbitrary precision. The program is included in the Appendix. The program was initially written to sum over a loop of every coordinate in the source and detection volumes. It was realized that MATLAB works better with vectorized calculations rather than with loops, so the program was re-written in the form of matrices. The script speed was increased by a couple of orders of magnitude, but there is undoubtedly more progress that could be made. On a moderately-powered home laptop PC the calculation takes about 5 seconds for a resolution of about 8000 voxels for the source volume.

In order to run the program, the user simply needs to change the field under "USER INPUTS" to his or her desired prepolarizing field, grain coarseness and detector location. The script, as it currently stands, will only calculate the magnetic

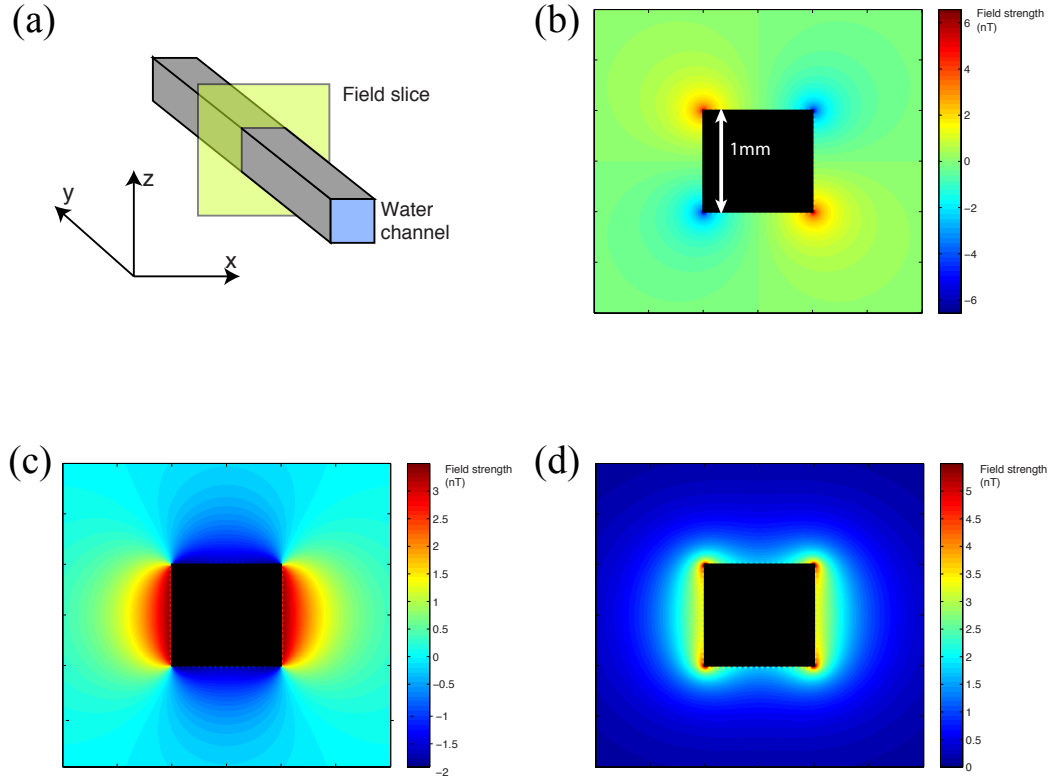


Figure 4.14: (a) Diagram of the field map geometry (b) x component of magnetic field (c) z component of magnetic field (d) magnitude of magnetic field. NB due to the geometry of the simulation the y component of the field was zero at all points

field around square prismatic structures. It is, however, simple to extend this to more complex shapes; indeed the program was initially written to examine the dipolar field from spheres and cones.

Using "dipolar field calculator", it was possible to calculate what kind of magnetic fields to expect from a sample of prepolarized water and thus determine what the sensitivity was necessary for this experiment. We envision a detector region consisting of a water channel about 1 mm in diameter with the diamond placed on one of the walls (Figure 4.13). The detection region is continuously refreshed with polarized water flowing from a prepolarizing volume. In the lab we have access to a 2 T prepolarizing volume. Higher prepolarizing fields are hard to generate with permanent magnets as the remnant field of a rare earth magnet is about 2 T. In order to go above

this electromagnets are necessary.

If flow between prepolarizing volume and detection region is fast, then T_1 can be ignored and the assumption made that the water loses no polarization during travel. Under these circumstances the following field maps are obtained for the field around a 1 mm width microfluidic channel.

From the field simulations, we can expect the magnetic field to be in the region of 4-5 nT in the best-case scenario. Given the current estimated sensitivity of around 50-100 nT after 100 seconds of signal averaging, the magnetometer is just over an order of magnitude away from being able to detect thermally polarized water.

4.4 Prospects

It appears that detection of water is currently just out of reach of the diamond NV magnetometer as it currently stands. If the current sensitivity limit is, at best, 50 nG, then to observe, say, 5 nG will take 100 times more signal averaging. This becomes a 3 hour experiment. Over that timescale, very small fluctuations in laser power or magnetic field noise would wash out the tiny signal. A better direction is to try to eliminate sources of noise rather than increase signal averaging time. Laser noise is a serious limitation in this experiment. The OEM Laser Systems laser is designed mainly as a laser light show device and has the stability profile to match. We have been investigating purchasing of a more stable lab-grade laser in order to remove this noise source. It is also not clear that we are exciting the NV ensemble in the most efficient manner. Linear polarization of the laser light may allow us to pick out a particular NV orientation in order to reduce our linewidth.

Another way to remove noise from the experiment would be to set up a gradiometric measurement system. By exciting two regions on the same diamond simultaneously, one in the magnetic field of interest and one in the lab field, sources of common-mode noise can be removed from the experiment. This would significantly remove laser noise and noise from fluctuations in the lab field.

Ultimately, however, CW NV magnetometry is limited; by moving to a pulse-mode, quantum control methods become available in order to extend the sensitivity of a magnetometer by orders of magnitude. Instead of a CW microwave driving field, we can apply discrete pulses, analogous to pulse-mode NMR.

Before continuing with explanation, its important to note that in a 3-level system such as the ground state triplet of the NV, the terms 180 and 90 pulse are not as clearly defined as in a 2-level system. The projection of the magnetization vectors on the Bloch sphere no longer maps 1:1 onto real space. However, the gist of the terms still applies. For example, the excitation of a coherence from the $m_s=0$ level is still

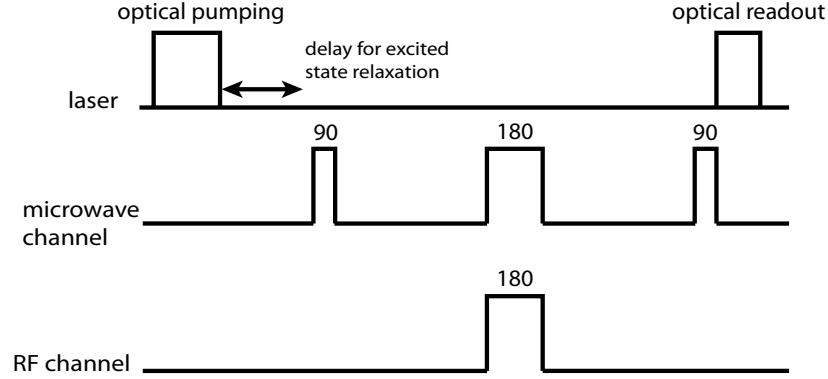


Figure 4.15: Spin echo pulse sequence suitable for pulsed NV magnetometry experiment

generally described as a 90 pulse.

A simple pulse base NV experiment begins with a 90 pulse exciting a coherence between the $|0\rangle$ and $|+\rangle$ state (where $|+\rangle = 1/\sqrt{2}(|+1\rangle + |-1\rangle)$) [59]. This superposition state evolves under local B-field, the kets developing a relative phase difference. This evolution is akin to the free induction decay in an NMR experiment, though unlike NMR, there's no direct way of measuring it. In order to observe this phase difference a second 90 pulse is used to turn the coherences back into populations. This population difference is probed by a laser pulse in the usual ODMR manner.

During the free evolution period of the experiment, the electron spins undergo T_2 decoherence. This limits the amount of time available to accrue phase and thus limits the sensitivity of the experiment. In order to lengthen the free evolution period, a single echo or train of echoes can be used to refocus the electron spins. The field being detected must also be flipped 180, however, or the accrued phase will unwind after the echo. If nuclear magnetization is being detected, this can be simply achieved by applying a pi pulse simultaneously with the microwave 90 pulse on the electrons. (Figure 4.15)

In a high N density diamond the relaxation time of the electrons is of the order of a few microseconds. Thus, the pulse sequences used to run these experiments need to be fast, both in the optical and microwave channels. In order to obtain maximum signal to noise, this pulse sequence must be repeated tens of thousands of times per second. This will require the purchasing a faster photodiode and DAC.

A CW laser can be used in a pulsed mode by passing the beam through an acousto-

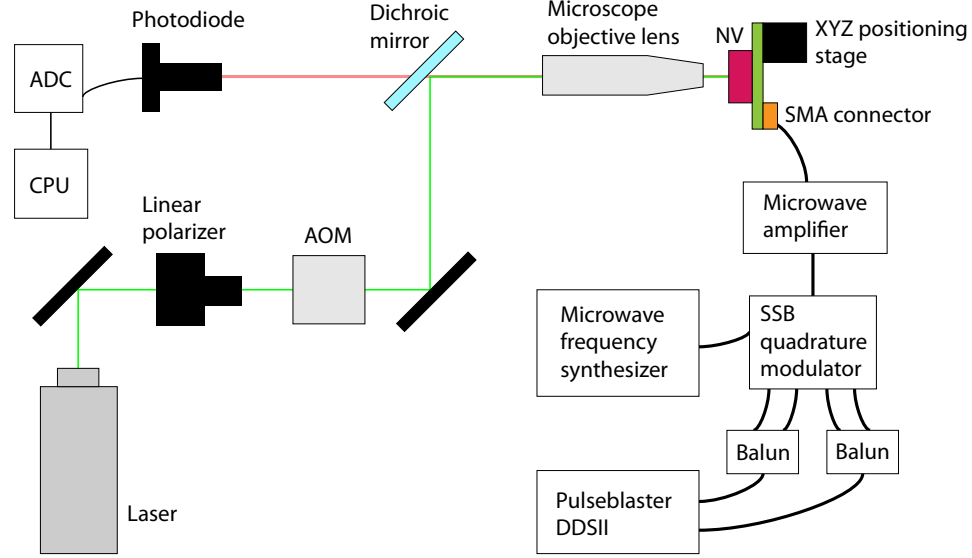


Figure 4.16: Block diagram of the pulsed NV magnetometry experiment

optic modulator (AOM). Radiofrequency oscillations in a crystal generate an effective diffraction grating, causing the light path to deviate on entering the crystal. The RF can be turned on or off, allowing pulses as short as a few nanoseconds to be generated.

Microwave pulse shaping and phase control for the pulsed experiments could be achieved through the use of an arbitrary waveform generator. However, these cost in the range of tens of thousands of dollars. Instead we have constructed a much cheaper alternative system, mixing a quadrature baseband RF signal, generated by a Spincore Pulseblaster DDSII, with the output of the PTS frequency synthesizer in a single-sideband microwave modulator (Analog Devices ADL 5373).

The experimental setup for the pulsed experiment is given in Figure 4.16. Currently experiments are ongoing in calibrating the response time of the AOM and the microwave output of the single-sideband microwave modulator. By moving to a pulsed-NMR approach, all of the advantages of quantum control will become available to us. Active decoupling of the NV center from paramagnetic impurities is a very exciting prospect which could help improve T_2 times significantly.

The future for this experiment is very bright. The results presented here are the fruits of barely 5 months of work. Already water detection is a very real possibility, and with orders magnitude improvements in sensitivity seemingly on a monthly basis, we may be able to look at more interesting spin systems in the near future. In the

longer term we are looking ahead to the construction of a scanning NV magnetometer in the same vein as Balasubramanian *et. al* [4]. The possibilities afforded to science by the operation of a working MR microscope are truly phenomenal; direct imaging of proteins, high resolution studies of cell mechanism and sub-surface catalysis studies are just some of the suggestions that are exciting the scientists in the NV community. If we can contribute just a little to this field then I feel that our work will have been worth every painstaking that I and my outstanding colleagues have spent.

Bibliography

- [1] V. Acosta, E. Bauch, M. Ledbetter, C. Santori, K.-M. Fu, P. Barclay, R. Beau-soleil, J. Roch, H. Linget, F. Treussart, S. Chemerisov, W. Gawlik, and D. Budker. Diamonds with a high density of nitrogen-vacancy centers for magnetometry applications. *Physical Review B*, 80(11):1–21, September 2009.
- [2] M S Albert, G D Cates, B. Driehuys, W. Happer, B. Saam, C S Springer, and A. Wishnia. Biological magnetic resonance imaging using laser-polarized ^{129}Xe . *Nature*, 370(6486):199–201, July 1994.
- [3] M V Balabas, K Jensen, W Wasilewski, H Krauter, L S Madsen, J H Müller, T Fernholz, and E S Polzik. High quality anti-relaxation coating material for alkali atom vapor cells. *Optics express*, 18(6):5825–30, March 2010.
- [4] Gopalakrishnan Balasubramanian, I Y Chan, Roman Kolesov, Mohannad Al-Hmoud, Julia Tisler, Chang Shin, Changdong Kim, Aleksander Wojcik, Philip R Hemmer, Anke Krueger, Tobias Hanke, Alfred Leitenstorfer, Rudolf Bratschitsch, Fedor Jelezko, and Jörg Wrachtrup. Nanoscale imaging magnetometry with diamond spins under ambient conditions. *Nature*, 455(7213):648–51, October 2008.
- [5] Gopalakrishnan Balasubramanian, Philipp Neumann, Daniel Twitchen, Matthew Markham, Roman Kolesov, Norikazu Mizuochi, Junichi Isoya, Jocelyn Achard, Johannes Beck, Julia Tisler, Vincent Jacques, Philip R Hemmer, Fedor Jelezko, and Jörg Wrachtrup. Ultralong spin coherence time in isotopically engineered diamond. *Nature materials*, 8(5):383–7, May 2009.
- [6] Brian Brocklehurst. Magnetic fields and radical reactions: recent developments and their role in nature. *Chemical Society Reviews*, 31(5):301–311, 2002.
- [7] K. Brownstein and C. Tarr. Importance of classical diffusion in NMR studies of water in biological cells. *Physical Review A*, 19(6):2446–2453, June 1979.
- [8] Bruker. *Paravision 4.0 A: Application Manual*. Bruker Biospin, 2006.

-
- [9] Dmitry Budker and Michael Romalis. Optical magnetometry. *Nature Physics*, 3(4):227–234, 2007.
- [10] HY Carr and EM Purcell. Effects of Diffusion on Free Precession in Nuclear Magnetic Resonance Experiments. *Physical Review*, 94(3):630638, 1954.
- [11] X.J. Chen, H.E. Möller, M.S. Chawla, G.P. Cofer, B. Driehuys, L.W. Hedlund, J.R. MacFall, and G.A. Johnson. Spatially resolved measurements of hyperpolarized gas properties in the lung in vivo. *Magnetic resonance in medicine*, 42(4):729737, 1999.
- [12] Luisa Ciobanu, Andrew G Webb, and Charles H Pennington. Signal enhancement by diffusion: experimental observation of the "DESIRE" effect. *Journal of magnetic resonance (San Diego, Calif. : 1997)*, 170(2):252–6, 2004.
- [13] PJ CONNOLLY and JC HOCH. Photochemical degradation of tryptophan residues during CIDNP experiments. *Journal of magnetic resonance*, 95(1):165173, 1991.
- [14] H B Dang, A C Maloof, and M V Romalis. Ultra-high sensitivity magnetic field and magnetization measurements with an atomic magnetometer. *arXiv:0910.2206v1 [physics.atom-ph]*, 2009.
- [15] C L Degen, M Poggio, H J Mamin, C T Rettner, and D Rugar. Nanoscale magnetic resonance imaging. *Proceedings of the National Academy of Sciences of the United States of America*, 106(5):1313–7, 2009.
- [16] V Demas. *No Ex-Situ NMR: Single Sided and Portable Magnetic Resonance Sensors*. Doctoral dissertation, University of California, Berkeley, 2006.
- [17] D. P. DiVincenzo. Quantum Computation. *Science*, 270(5234):255–261, 1995.
- [18] Jonathan P Dowling and Gerard J Milburn. Quantum technology: the second quantum revolution. *Philosophical transactions. Series A, Mathematical, physical, and engineering sciences*, 361(1809):1655–74, 2003.
- [19] Marco F Duarte, Mark A Davenport, Dharmpal Takhar, Jason N Laska, Ting Sun, Kevin F Kelly, and Richard G Baraniuk. Single-Pixel Imaging via Compressive Sampling. *IEEE Signal Processing Magazine, Special Issue on Compressive Sampling*, (March 2008):1–19.
- [20] PB Fernandes. Technological advances in high-throughput screening. *Current Opinion in Chemical Biology*, 1998.

-
- [21] J Frank. *The Design and Testing of RF Pulses to Encode Compensations and Perform Excitations in Inhomogeneous Fields*. Doctoral dissertation, University of California, Berkeley, 2008.
- [22] E Fukushima and S Roeder. *Experimental Pulse NMR: A Nuts and Bolts Approach*. Westview Press, 1986.
- [23] Martin Goez. *Annual Reports on NMR Spectroscopy Volume 66*, volume 66 of *Annual Reports on NMR Spectroscopy*. Elsevier, 1 edition, 2009.
- [24] Martin Goez, Ilya Kuprov, and P J Hore. Increasing the sensitivity of time-resolved photo-CIDNP experiments by multiple laser flashes and temporary storage in the rotating frame. *Journal of magnetic resonance (San Diego, Calif. : 1997)*, 177(1):139–45, November 2005.
- [25] A. Gruber. Scanning Confocal Optical Microscopy and Magnetic Resonance on Single Defect Centers. *Science*, 276(5321):2012–2014, 1997.
- [26] E. Hahn. Spin Echoes. *Physical Review*, 80(4):580–594, 1950.
- [27] E Hahn. Personal correspondence, 2010.
- [28] Elad Harel and Alex Pines. Spectrally resolved flow imaging of fluids inside a microfluidic chip with ultrahigh time resolution. *Journal of magnetic resonance (San Diego, Calif. : 1997)*, 193(2):199–206, 2008.
- [29] JB Hartle and SW Hawking. Wave function of the universe. *Physical Review D*, 28(12):29602975, 1983.
- [30] PJ Hore and RW Broadhurst. Photo-CIDNP of biopolymers. *Progress in nuclear magnetic resonance spectroscopy*, 25(4):345402, 1993.
- [31] M D Hürlimann. Diffusion and relaxation effects in general stray field NMR experiments. *Journal of magnetic resonance (San Diego, Calif. : 1997)*, 148(2):367–78, 2001.
- [32] M D Hürlimann, M Flaum, L Venkataramanan, C Flaum, R Freedman, and G J Hirasaki. Diffusion-relaxation distribution functions of sedimentary rocks in different saturation states. *Magnetic resonance imaging*, 21(3-4):305–10, 2002.
- [33] F Jelezko, T Gaebel, I Popa, A Gruber, and J Wrachtrup. Observation of coherent oscillations in a single electron spin. *Physical review letters*, 92(7):76401, 2004.
- [34] R Kaptein, K Dijkstra, and K Nicolay. Laser photo-CIDNP as a surface probe for proteins in solution. *Nature*, 274:293–294, 1978.

- [35] John Kitching, Svenja Knappe, W. Clark Griffith, Jan Preusser, Vladislav Gerginov, Peter D. D. Schwindt, Vishal Shah, and Ricardo Jimenez-Martinez. Uncooled, millimeter-scale atomic magnetometers with femtotesla sensitivity. *2009 IEEE Sensors*, pages 1844–1847, October 2009.
- [36] Eriks Kupce and Ray Freeman. Two-dimensional Hadamard spectroscopy. *Journal of Magnetic Resonance*, 162(2):300–310, June 2003.
- [37] P. C. Lauterbur. Image Formation by Induced Local Interactions: Examples Employing Nuclear Magnetic Resonance. *Nature*, 242(5394):190–191, 1973.
- [38] M P Ledbetter, I M Savukov, D Budker, V Shah, S Knappe, J Kitching, D J Michalak, S Xu, and a Pines. Zero-field remote detection of NMR with a microfabricated atomic magnetometer. *Proceedings of the National Academy of Sciences of the United States of America*, 105(7):2286–90, February 2008.
- [39] S.-K. Lee, K. L. Sauer, S. J. Seltzer, O. Alem, and M. V. Romalis. Subfemtotesla radio-frequency atomic magnetometer for detection of nuclear quadrupole resonance. *Applied Physics Letters*, 89(21):214106, 2006.
- [40] Daniel Loss. Quantum phenomena in Nanotechnology. *Nanotechnology*, 20(43):430205, 2009.
- [41] Kiminori Maeda, Kevin B. Henbest, Filippo Cintolessi, Ilya Kuprov, Christopher T. Rodgers, Paul A. Liddell, Devens Gust, Christiane R. Timmel, and P. J. Hore. Chemical compass model of avian magnetoreception. *Nature*, 453(7193):387–390, April 2008.
- [42] N Manson. Personal correspondence, 2010.
- [43] C Massin. Planar microcoil-based microfluidic NMR probes. *Journal of Magnetic Resonance*, 164(2):242–255, October 2003.
- [44] E.E. McDonnell, S.I. Han, C. Hilty, K. Pierce, and A. Pines. NMR analysis on microfluidic devices by remote detection. *Lawrence Berkeley National Laboratory: Lawrence Berkeley National Laboratory. LBNL Paper LBNL-58631*, 2005.
- [45] K Hun Mok, Toshio Nagashima, Iain J Day, Jonathan A Jones, Charles J V Jones, Christopher M Dobson, and P J Hore. Rapid sample-mixing technique for transient NMR and photo-CIDNP spectroscopy: applications to real-time protein folding. *Journal of the American Chemical Society*, 125(41):12484–92, October 2003.

-
- [46] H.E. Möller, M.S. Chawla, X.J. Chen, B. Driehuys, L.W. Hedlund, C.T. Wheeler, and G.A. Johnson. Magnetic resonance angiography with hyperpolarized ^{129}Xe dissolved in a lipid emulsion. *Magnetic Resonance in Medicine*, 41(5):1058–1064, 1999.
- [47] S Mueller. *Upgrading and Repairing PCs*. Que, 19th edition, 2009.
- [48] M A Nielsen and I L Chuang. *Quantum Computation and Quantum Information*. Cambridge University Press, 1st edition, 2000.
- [49] J Paulsen. *The Design and Application of an Adjustable NMR Sensor and the MRI Imaging of flow in Microfluidics With Remote Detection*. Doctoral dissertation, University of California, Berkeley, 2009.
- [50] NJ Pienta and DW Smith. Versatile light guide design for ultraviolet light photo-CIDNP experiments. Modification of a Varian EM-360. *Journal of Magnetic Resonance*, 63(2):380–382, 1985.
- [51] Christopher T Rodgers and P J Hore. Chemical magnetoreception in birds: The radical pair mechanism. *Proceedings of the National Academy of Sciences*, 106(2):353–360, 2009.
- [52] M. Romalis and M. Ledbetter. Transverse Spin Relaxation in Liquid ^{129}Xe in the Presence of Large Dipolar Fields. *Physical Review Letters*, 87(6):3–6, 2001.
- [53] D Rugar, R Budakian, H J Mamin, and B W Chui. Single spin detection by magnetic resonance force microscopy. *Nature*, 430(6997):329–32, July 2004.
- [54] LD Schearer and GK Walters. Nuclear Spin-Lattice Relaxation in the Presence of Magnetic-Field Gradients. *Physical Review*, 139(5A):A1398–A1402, August 1965.
- [55] J.A. Seeley, S.I. Han, and A. Pines. Remotely detected high-field MRI of porous samples. *Journal of Magnetic Resonance*, 167(2):282–290, 2004.
- [56] Wenjin Shao, Guodong Wang, Raymond Fuzesy, Emlyn W. Hughes, Blaine A. Chronik, Greig C. Scott, Steven M. Conolly, and Albert Macovski. Low readout field magnetic resonance imaging of hyperpolarized xenon and water in a single system. *Applied Physics Letters*, 80(11):2032, 2002.
- [57] Boaz Shapira, Erel Morris, Karol A Muszkat, and Lucio Frydman. Sub-second 2D NMR spectroscopy at sub-millimolar concentrations. *Journal of the American Chemical Society*, 126(38):11756–7, September 2004.

- [58] T. Su, G. L. Samuelson, S. W. Morgan, G. Laicher, and B. Saam. Liquid hyperpolarized [sup 129]Xe produced by phase exchange in a convection cell. *Applied Physics Letters*, 85(12):2429, 2004.
- [59] J. M. Taylor, P. Cappellaro, L. Childress, L. Jiang, D. Budker, P. R. Hemmer, a. Yacoby, R. Walsworth, and M. D. Lukin. High-sensitivity diamond magnetometer with nanoscale resolution. *Nature Physics*, 4(10):810–816, 2008.
- [60] I Tkác, Z Starcuk, I Y Choi, and R Gruetter. In vivo 1H NMR spectroscopy of rat brain at 1 ms echo time. *Magnetic resonance in medicine : official journal of the Society of Magnetic Resonance in Medicine / Society of Magnetic Resonance in Medicine*, 41(4):649–56, April 1999.
- [61] D R Trease, V S Bajaj, J Paulsen, and A Pines. Ultrafast optical encoding of magnetic resonance. *Submitted*, 2010.
- [62] C. Tseng, R. Mair, G. Wong, D. Williamson, D. Cory, and R. Walsworth. Magnetic resonance imaging of laser polarized liquid xenon. *Physical Review E*, 59(2):1785–1788, February 1999.
- [63] Y Tsentalovich. Laser flash photolysis and time resolved CIDNP study of photoreaction of 2,2-dipyridyl with N-acetyl tyrosine in aqueous solutions. *Journal of Photochemistry and Photobiology A: Chemistry*, 131(1-3):33–40, February 2000.
- [64] Yuri P. Tsentalovich, Olga B. Morozova, Alexandra V. Yurkovskaya, and P. J. Hore. Kinetics and Mechanism of the Photochemical Reaction of 2,2-Dipyridyl with Tryptophan in Water: Time-Resolved CIDNP and Laser Flash Photolysis Study. *The Journal of Physical Chemistry A*, 103(27):5362–5368, July 1999.
- [65] Yuri P. Tsentalovich, Olga B. Morozova, Alexandra V. Yurkovskaya, P. J. Hore, and Renad Z. Sagdeev. Time-Resolved CIDNP and Laser Flash Photolysis Study of the Photoreactions of N -Acetyl Histidine with 2,2-Dipyridyl in Aqueous Solution. *The Journal of Physical Chemistry A*, 104(30):6912–6916, August 2000.
- [66] Robert Tycko and Jeffrey A Reimer. Optical Pumping in Solid State Nuclear Magnetic Resonance. *Journal of Physical Chemistry*, 100(31):13240–13250, 1996.
- [67] T.G. Walker and W. Happer. Spin-exchange optical pumping of noble-gas nuclei. *Reviews of Modern Physics*, 69(2):629642, 1997.
- [68] Jamie Walls, Frederick Phoa, and Yung-Ya Lin. Spin dynamics at very high spin polarization. *Physical Review B*, 70(17):1–8, 2004.
- [69] H.R. Ward and R.G Lawler. Nuclear magnetic resonance emission and enhanced absorption in rapid organometallic reactions. *Journal of the American Chemical Society*, 89(21):5518–5519, 1967.

-
- [70] Shoujun Xu, C. Crawford, Simon Rochester, Valeriy Yashchuk, Dmitry Budker, and Alexander Pines. Submillimeter-resolution magnetic resonance imaging at the Earth's magnetic field with an atomic magnetometer. *Physical Review A*, 78(1):2–5, 2008.
- [71] X Xu, D R Trease, L-S Bouchard, N Halpern-Manners, D Graziani, and A Pines. Probing surface relaxivity of solid materials using xenon NMR. *Unpublished Results*, 2010.
- [72] W. Yen and R. Norberg. Nuclear Magnetic Resonance of Xe129 in Solid and Liquid Xenon. *Physical Review*, 131(1):269–275, July 1963.
- [73] Martin G. Zysmilich and Ann McDermott. Photochemically Induced Dynamic Nuclear Polarization in the Solid-State ^{15}N Spectra of Reaction Centers from Photosynthetic Bacteria *Rhodobacter sphaeroides* R-26. *Journal of the American Chemical Society*, 116(18):8362–8363, September 1994.

Appendix A

Appendix

A.1 Dipole field caculator

```

clear all;
close all;

% USER INPUTS %%%%%%%%%%%%%%

matrixx    = 20;      %source matrix elements in x dimension
matrixy    = 20;      %source matrix elements in y dimension
matrixz    = 20;      %source matrix elements in z dimension

lengthx    = 0.001;   %source length along x  (in m)
lengthy    = 0.001;   %source length along y  (in m)
lengthz    = 0.001;   %source length along z  (in m)

\% Detector dimensions

t_matx     = 280;      %detector matrix elements in x dimension
t_maty     = 1;        %detector matrix elements in y dimension
t_matz     = 280;      %detector matrix elements in z dimension

t_lenx     = 0.0014;   %detector length along x  (in m)
t_leny     = 0.0010;   %detector length along y  (in m)

```

```

t_lenz      = 0.0014;    %detector length along z   (in m)

t_corner    = [-0.0002,0,-0.0002];    %corner of the detector matrix(x,y,z)
% the corner origin of the channel is arbitrarily assigned as [0,0,0]

T    = 298;              %temperature
B_0  = 2                  %prepolarizing field strength

% END OF USER INPUTS %%%%%%%%%%%%%%

resx      = lengthx/matrixx;    %source resolution in x
resy      = lengthy/matrixy;    %source resolution in y
resz      = lengthz/matrixz;    %source resolution in z
v          = resx*resy*resz;    %volume of voxel;

t_resx     = t_lenx/t_matx;     %target resolution
t_resy     = t_leny/t_maty;
t_resz     = t_lenz/t_matz;

%%%%%%%%%%%%%

% fundamental constants %%

Na  = 6.022e23;            %avogadro's number
conc= 110;                %concentration of protons in water (moles/dm^3)

h    = 6.6260755e-34;     %h
hba  = h/(2*pi);          %hbar
u0   = pi*4e-7;           %mu
gy_H = 42.576*pi*2e6;     %proton gyromagnetic ratio
k    = 1.381e-23;         %Boltzmann constant
u0   = pi*4e-7;           %magnetic constant, mu0
uH   = 14.106067e-27;     %proton magnetic moment

n    = 110*6.022e23;      %number of protons in 1 dm^3 H2O
vd   = v*10^3;           %volume of one voxel (dm^3)
n_v  = vd*n;             %number of protons per voxel

pol  = hba*gy_H*B_0/(2*k*T) %nuclear polarization
M    = uH*n_v*pol;        %magnetization per voxel

```

```

C    = (u0/(4*pi))*(3*M); %constants in calculation

% Generate the source array

S = zeros(matrixx,matrixy,matrixz,4); %this is the field source array

for y=1:matrixy;
    for z=1:matrixz;
        S(1:matrixx,y,z,1)=(1:matrixx)-0.5;
    end
end

for x=1:matrixx;
    for z=1:matrixz;
        S(x,1:matrixy,z,2)=(1:matrixy)-0.5;
    end
end

for x=1:matrixx;
    for y=1:matrixy;
        S(x,y,1:matrixz,3)=(1:matrixz)-0.5;
    end
end

% The coords of each voxel are now placed in the source matrix. The coords
% are set so that the voxel is centered halfway between each integer.

% We now scale the source matrix. This is a matrix where 1,1,1,1 is the x
% coordinate of the 1,1,1 element. 1,1,1,2 is the y coordinate, etc. It is
% constructed to make calculation lots faster

S(:, :, :, 1) = S(:, :, :, 1)*resx;
S(:, :, :, 2) = S(:, :, :, 2)*resy;
S(:, :, :, 3) = S(:, :, :, 3)*resz;

% Now we have our generic source matrix

T=zeros(t_matx,t_matz,4); %this is the matrix of field strengths

```

```

% Here we choose a y-slice for detection

yt = t_maty/2;          %yt in arbit units
ytpos = yt*t_resy;      %yt relative to corner (m)
yt_abs = ytpos+t_corner(2);

for xt=1:t_matx;          %picks out a single voxel from the target array
    % ie 1-20
    disp(xt);             %displays how far we've got in the calcn
    xtpos = (xt-0.5)*t_resx; % gives the coordinates of the center
    % ie 0.5-19.5 * resolution
    xt_abs = xtpos+t_corner(1); % gives the the absolute position of xt
    % ie x position relative to corner + corner relative to origin

    for zt=1:t_matz;
        ztpos = (zt-0.5)*t_resz;
        zt_abs = ztpos+t_corner(3);

        S_curr(:,:,:,1) = S(:,:,:,1)-xt_abs;
        S_curr(:,:,:,2) = S(:,:,:,2)-yt_abs;
        S_curr(:,:,:,3) = S(:,:,:,3)-zt_abs;

        S_curr(:,:,:,4) = (S_curr(:,:,:,1).^2+S_curr(:,:,:,2).^2+
            S_curr(:,:,:,3).^2); %the denominator (r^2)
        S_curr(:,:,:,5) = (S_curr(:,:,:,1).*S_curr(:,:,:,3))./
            S_curr(:,:,:,4).^(5/2); %for Bx
        S_curr(:,:,:,6) = (S_curr(:,:,:,2).*S_curr(:,:,:,3))./
            S_curr(:,:,:,4).^(5/2); %for By
        S_curr(:,:,:,7) = (S_curr(:,:,:,3).^2 - ((1/3)*
            S_curr(:,:,:,4)))./S_curr(:,:,:,4).^(5/2); %for Bz

        %now we sum over all the individual components from each
        %spin voxel

        totalsx = sum(S_curr(:,:,:,5));
        totalsx = sum(totalsx);
        totalsx = sum(totalsx);

        T(xt,zt,1)=C*totalsx;
    end
end

```



```
        totalsy = sum(S_curr(:,:, :,6));
        totalsy = sum(totalsy);
        totalsy = sum(totalsy);

        T(xt,zt,2)=C*totalsy;

        totalsz = sum(S_curr(:,:, :,7));
        totalsz = sum(totalsz);
        totalsz = sum(totalsz);

        T(xt,zt,3)=C*totalsz;

        T(xt,zt,4)=(T(xt,zt,1)^2 + T(xt,zt,2)^2 +
                    T(xt,zt,3)^2)^(1/2);

    end
end

figure(1);
imagesc(T(:,:,1)); title('x field component'), colorbar;

figure(2);
imagesc(T(:,:,2)); title('y field component'), colorbar;

figure(3);
imagesc(T(:,:,3)); title('z field component'), colorbar;

figure(4);
imagesc(T(:,:,4)); title('magnitude'), colorbar;
```